nature cardiovascular research

Article

https://doi.org/10.1038/s44161-024-00532-x

Tissue-resident memory T cells in epicardial adipose tissue comprise transcriptionally distinct subsets that are modulated in atrial fibrillation

Received: 20 September 2023

Accepted: 29 July 2024

Published online: 23 August 2024

Check for updates

Vishal Vyas[1,2], Balraj Sandhar[1], Jack M. Keane[1], Elizabeth G. Wood[1], Hazel Blythe[1], Aled Jones[1], Eriomina Shahaj[1], Silvia Fanti[1], Jack Williams[1], Nasrine Metic[3], Mirjana Efremova[3], Han Leng Ng[4], Gayathri Nageswaran[5], Suzanne Byrne[5], Niklas Feldhahn[4], Federica Marelli-Berg[1], Benny Chain[5], Andrew Tinker[1], Malcolm C. Finlay[1,2] & M. Paula Longhi[1]

Atrial fibrillation (AF) is the most common sustained arrhythmia and carries an increased risk of stroke and heart failure. Here we investigated how the immune infiltrate of human epicardial adipose tissue (EAT), which directly overlies the myocardium, contributes to AF. Flow cytometry analysis revealed an enrichment of tissue-resident memory T (T_{RM}) cells in patients with AF. Cellular indexing of transcriptomes and epitopes by sequencing (CITE-seq) and single-cell T cell receptor (TCR) sequencing identified two transcriptionally distinct $CD8^+$ T_{RM} cells that are modulated in AF. Spatial transcriptomic analysis of EAT and atrial tissue identified the border region between the tissues to be a region of intense inflammatory and fibrotic activity, and the addition of T_{RM} populations to atrial cardiomyocytes demonstrated their ability to differentially alter calcium flux as well as activate inflammatory and apoptotic signaling pathways. This study identified EAT as a reservoir of T_{RM} cells that can directly modulate vulnerability to cardiac arrhythmia.

Atrial fibrillation (AF) is the most common sustained arrhythmia worldwide, defined by rapid, uncoordinated atrial activity with consequent deterioration of atrial mechanical function[1]. Patients suffering from AF have poorer outcomes in heart failure, an increased risk of cognitive decline and vascular dementia as well as a five-fold increased risk of stroke[2,3]. The financial costs are commensurate with this health burden, with over £2 billion spent annually in healthcare costs within England alone[4].

The exact etiology of AF remains incompletely understood, requiring complex interactions between triggers and the underlying atrial substrate to sustain AF. Inflammation is known to play a key role in the formation of AF substrate, promoting electrical and structural remodeling of the atrium and increasing vulnerability to AF[5]. Several studies described an association between AF and serum inflammatory biomarkers, such as C-reactive protein (CRP) and IL-6 (refs. 6,7). However, only a limited number of studies have looked at the immune infiltrate in the atrial tissue itself. Abnormal atrial histology, characterized by inflammatory infiltrates, fibrosis and expression of pro-inflammatory cytokines, has been identified in tissue biopsies of patients with AF[8–11].

[1]William Harvey Research Institute, Barts and The London School of Medicine and Dentistry, Queen Mary University of London, London, UK. [2]Department of Cardiology, Barts Heart Centre, St. Bartholomew's Hospital, London, UK. [3]Cancer Research UK, Barts Centre, Queen Mary University of London, London, UK. [4]Department of Immunology and Inflammation, Centre for Haematology, Faculty of Medicine, Imperial College London, London, UK. [5]UCL Division of Infection and Immunity, University College London, London, UK. e-mail: m.longhi@qmul.ac.uk

However, the patient numbers and range of tissue analyses in these studies remain limited.

Numerous lines of evidence suggest a role of epicardial adipose tissue (EAT) in the development of AF. EAT is the visceral fat depot of the heart that shares direct anatomic contact with the myocardium without fascial interruption. EAT has been demonstrated to be a significant source of inflammatory mediators that can exert paracrine and vasocrine effects on the myocardium[12]. Several observational studies have demonstrated that EAT volume is consistently associated with the presence, severity and recurrence of AF[13–15]. Furthermore, increased EAT inflammation, as measured by ^{18}F-fluorodeoxyglucose (FDG) uptake, was observed in patients with AF compared to those in sinus rhythm (SR)[16,17]. A range of pathophysiological mechanisms could contribute to the association between EAT and AF, including adipocyte infiltration, oxidative stress and the paracrine effect of pro-fibrotic and pro-inflammatory cytokines. However, the exact immune structure and cellular characterization of EAT in AF remains elusive.

In the present study, we investigated the pathophysiological significance of the immune infiltrate in the EAT of patients with AF. Flow cytometry analysis identified an enrichment of tissue-resident memory T (T_{RM}) cells in patients with AF compared to SR controls. T_{RM} cells are a specialized subset of memory T cells that persist long term in peripheral tissues with minimal recirculation. To further characterize these cells, we applied cellular indexing of transcriptomes and epitopes by sequencing (CITE-seq) combined with single-cell T cell receptor (TCR) sequencing, which identified two transcriptionally distinct $CD8^+$ T_{RM} cells that are modulated in AF. Furthermore, spatial transcriptomic analysis of the border zone between the EAT and the atrial, together with functional analysis, suggests that EAT is a reservoir of T_{RM} cells that can serve as mediators of inflammation in the myocardium.

Table 1 | Clinical characteristic of patients with AF and on SR

	Pre-existing AF (*n*=18)	SR (*n*=26)	*P* value
Age (years)	67.3±7.8	65.6±8.8	0.47
Male gender (%)	14 (78)	17 (65)	0.51
BMI (kg m^{-2})	26.6±4.5	26.8±3.9	0.91
Diabetes (%)	2 (11)	3 (12)	0.99
Hypertension (%)	12 (67)	18 (67)	0.99
Hyperlipidaemia (%)	11 (61)	16 (61)	0.99
Smoking history (%)	8 (44)	13 (50)	0.59
Prior myocardial infarction (%)	3 (17)	7 (27)	0.49
Left ventricular ejection fraction (%)	59 (55–63)	60 (58–61)	0.49
Preoperative use of beta-blockers (%)	11 (61)	12 (46)	0.37
Preoperative use of statins (%)	12 (67)	17 (65)	0.99
Preoperative CRP (mg l^{-1})	0 (0–5)	0 (0–9)	0.69
Preoperative neutrophil:lymphocyte	2.6 (1.8–4.2)	2.6 (1.9–3.4)	0.62
Left atrial size (cm)	4.9±1.5	3.6±0.6	0.03*
Coronary artery bypass surgery (%)	9 (50)	50 (67)	0.99
Valve surgery (%)	10 (56)	15 (58)	0.99
Combination coronary artery bypass/ valve surgery (%)	3 (17)	3 (12)	0.68

Two-tailed Student's *t*-test/Mann–Whitney test for continuous data or χ^2/Fisher's exact test for categorical data was used where appropriate. *P<0.05.

Results

T_{RM} cells are increased in the EAT of patients with AF

A total of 153 participants undergoing open heart surgery were recruited to this study. The mean age was 66.1 years, with a mean body mass index (BMI) of 28.2 kg m^{-2}, and 75% of participants were male, with 50% undergoing a coronary artery bypass surgery (Supplementary Table 1). To evaluate the immune profile of the EAT in AF, participants were classified into two groups based on their 12-lead electrocardiogram (ECG)-confirmed rhythm, recorded preoperatively: AF or those in normal rhythm (SR). Thirty-one participants developed postoperative AF and were, therefore, excluded from the study. Patients with AF were older and more likely to undergo valve surgery (Supplementary Table 2). As expected, patients with AF had a more dilated left atrium, as previously described, as a result of tissue remodeling[18]. Thus, to account for key variables, we performed propensity score matching with age, gender, BMI, diabetes, hypertension and procedure type as covariates (Table 1). Key immune cells were identified by flow cytometry in the EAT, in subcutaneous adipose tissue (SAT) as a control adipose tissue and in blood as a marker of the systemic inflammatory state. No differences were observed in cell number between the groups and across the tissues (Extended Data Fig. 1a–d). The frequencies of myeloid and lymphoid cells were largely unchanged with the exception of a decrease in $CD14^+CD206^+$ macrophages and an increase in total $CD3^+$ T cells in patients with AF (Extended Data Fig. 1e). We previously showed that T cells are a predominant immune cell constituent in human EAT[19]. Analysis of T cell subsets identified an increase in T_{RM} cells, as defined by high expression of CD69 and the inhibitory molecule programmed cell death 1 (PD1) receptor, in the EAT of patients with AF compared to SR (Fig. 1a and Extended Data Fig. 2a), which was accompanied by a decrease in $CD69^-$ memory T cells (Extended Data Fig. 1e). The increase in T_{RM} cells was readily evident in unmatched participants and independent of risk factors, such as age, hypertension and body weight (Extended Data Fig. 2b–e). T_{RM} cells are transcriptionally programmed for strong effector function to confer swift on-site

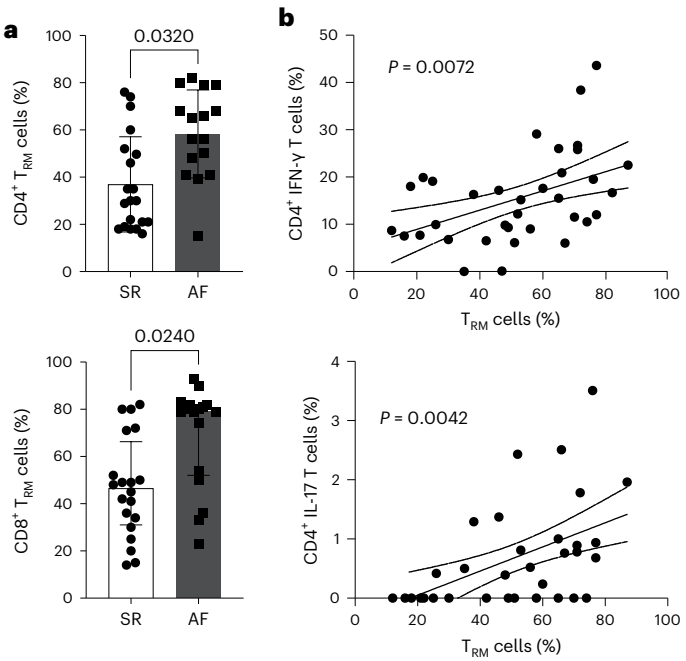

Fig. 1 | Evaluation of T_{RM} cell frequency in EAT. EAT immune infiltrate from patients with AF or patients in SR was characterized by flow cytometry. **a**, Bar graphs indicate the frequency of $CD4^+$ and $CD8^+$ T_{RM} cells over total $CD4^+$ or $CD8^+CD45RO^+$ T cells, respectively, in the EAT (n = 26 SR and n = 18 AF biological replicates). Statistical significance was determined using unpaired two-tailed *t*-test for the parametrically distributed groups. Data are represented as mean ± s.d. **b**, Cytokine production was evaluated by intracellular staining by flow cytometry. Correlation analysis of IFN-γ and IL-17 production with the frequency of $CD4^+$ T_{RM} cells measured by linear regression. Graphs show 95% confidence bands (r = 0.299) and two-tailed P value analysis. All data show individual patients (n = 44).

https://doi.org/10.1038/s44161-024-00532-x

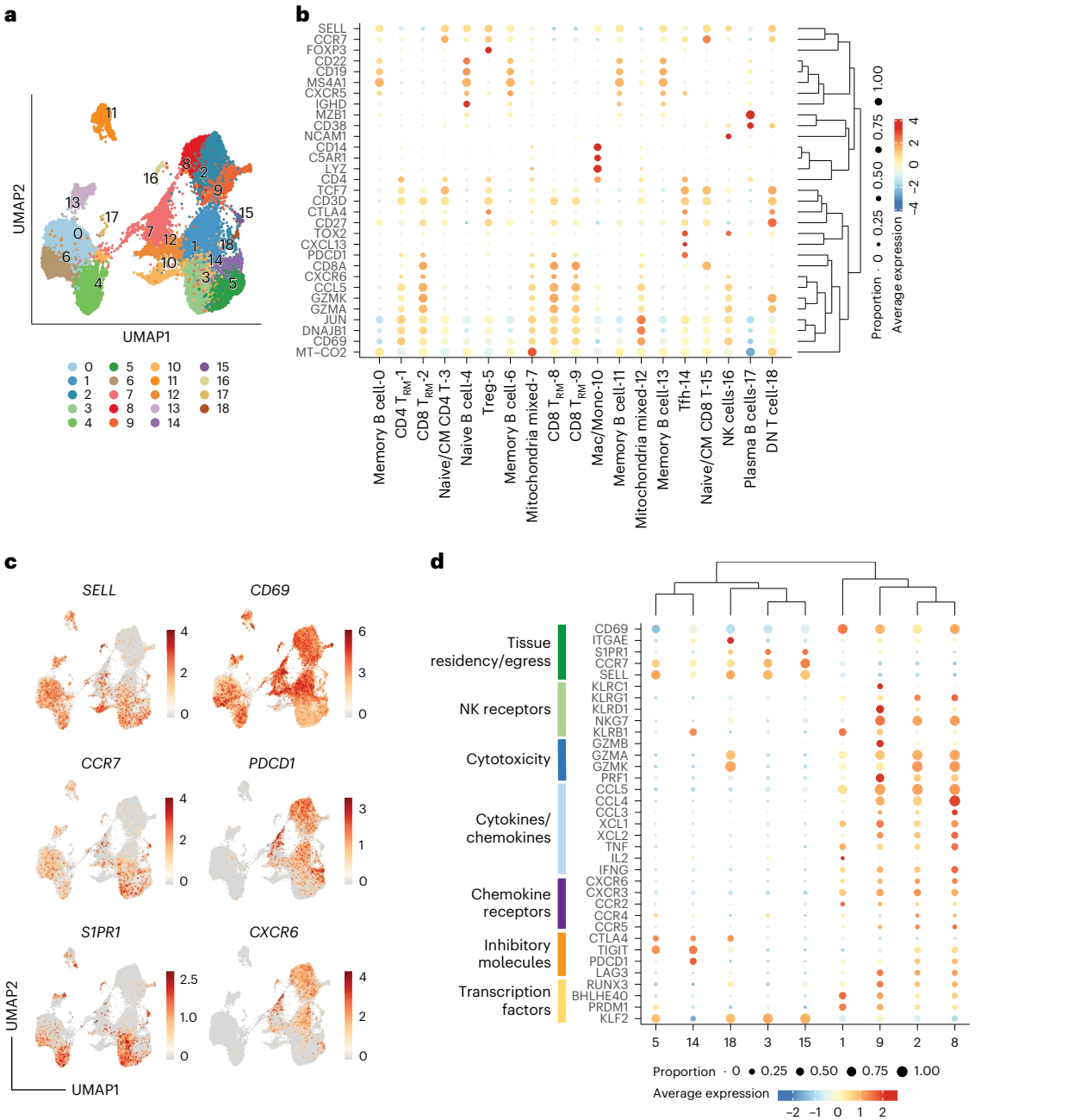

Fig. 2 | CITE-seq analysis of immune cells in the EAT and AA. a, UMAP plots of merged EAT and AA samples identified 19 cell clusters. **b**, Bubble plot shows expression levels of representative markers within each cluster. **c**, Canonical markers used to identify T_{RM} cells are represented in the UMAP plot. Data are colored according to average expression levels. Expression values are normalized for quantitative comparison within each dataset. **d**, Bubble plot showing the expression distribution of effector molecules, receptors and transcription factors among T cell populations. DN, double-negative.

immune protection[20]. We then evaluated T cell cytokine production by intracellular staining. The gating strategy is shown in Extended Data Fig. 2f,g. A clear correlation between IFN-γ and IL-17 production and the presence of $CD4^+$ T_{RM} cells was observed (Fig. 1b). No such correlation was detected for IFN-γ and $CD8^+$ T_{RM} cells, which could be attributed to the high cytotoxic activity of these cells (Extended Data Fig. 2h,i). Overall, our data suggest that T_{RM} cells could play a pathological role in the development and/or persistence of AF.

EAT serves as a reservoir of T_{RM} cells

T_{RM} cells are transcriptionally, phenotypically and functionally distinct from other memory T cell populations. T_{RM} cells can be identified in tissue by their expression of CD69 and a core gene signature shared between $CD4^+$ and $CD8^+$ T_{RM} cells in multiple lymphoid and mucosal sites[20]. However, to establish long-term residency in different tissues, T_{RM} cells are required to display tissue-specific transcriptional features to accommodate unique local environmental cues[21]. To confirm the identity of $CD69^+PD1^+$ cells identified by flow cytometry, we performed CITE-seq profiling of immune cells within the EAT from two patients with AF. CITE-seq allows optimal annotation of cell populations and identification of protein isoforms, such as the canonical memory marker CD45RO, that cannot be identified by RNA sequencing (RNA-seq) alone[22]. In addition, to explore the interrelationship between T cells in the EAT and underlying myocardium, given the anatomical intimacy between these two tissues, we transcriptionally profiled paired EAT and atrial appendage (AA) samples. To improve sensitivity, given

https://doi.org/10.1038/s44161-024-00532-x

that immune cells comprise a relatively small proportion of cells in the EAT and AA, CITE-seq was performed on sorted CD45$^+$ cells. Unsupervised clustering and uniform manifold approximation and projection (UMAP) dimensionality reduction from 28,242 cells across the two paired EAT and RAA samples yielded 19 clusters that were annotated based on the expression of data-driven marker genes (Fig. 2a). Similar clusters could be observed in the EAT and paired AA, with a clear enrichment of adaptive immune cells, consistent with our previous work (Extended Data Fig. 3a)[19].

Differential gene expression from the CITE-seq data resolved T cell subsets into nine clusters (Fig. 2a,b and Supplementary Table 3). CD4$^+$ T cells comprised four clusters: a distinct T_{RM} cluster expressing the canonical markers *CD69*, *PDCD1* and *CXCR6* and low *CCR7* and *SELL* expression (cluster 1); naive or T central memory (T_{CM}) cells expressing

Fig. 3 | Characterization of T_{RM} cells across EAT and AA tissues. a, Volcano plots showing the average log fold changes and average Benjamini–Hochberg-corrected *P* values for pairwise differential expression between EAT and AA tissues for all T_{RM} cluster populations based on the non-parametric Wilcoxon rank-sum test. **b**, Expression of surface CD107a was analyzed on activated $CD8^+$ T_{RM} cells by flow cytometry. Bar graph indicates the percentage of $CD107a^+CD8^+$ T_{RM} cells in paired EAT and AA samples. Data are presented as mean ± s.d. Statistical significance was determined using paired two-tailed *t*-test ($n = 3$ biological replicates). **c**, UMAP visualization of clonotype expansion levels among clusters. Data are colored according to clonal expansion levels. **d**, Clonal expansion levels of T cell clusters quantified by STARTRAC-expa indices for each sample. Statistical significance was determined using the Kruskal–Wallis test with Dunn's multiple comparisons test ($n = 4$ biological replicates) **e**, Migration potential of T cell clusters quantified by STARTRAC-migr indices for each patient. Statistical significance was determined using one-way ANOVA with Tukey's multiple comparisons test ($n = 2$ biological replicates). Box plots in **d** and **e** show data points from individual tissues with means and minimum/maximum values. **f**, Volcano plots showing the average log fold changes and average Benjamini–Hochberg-corrected *P* values for pairwise differential expression between hyperexpanded TCR clones in the EAT and AA tissues. **g**, Bar graph indicates the relative abundance of TCRα clonotypes in paired tissues EAT, AA and blood (BLD) ($n = 5$ biological replicates). The relative abundance of TCRα clonotypes was calculated using the Immunarch package in R (version 1.0.0) and grouped accordingly as rare, small, medium, large and hyperexpanded. Data are presented as mean ± s.d. Statistical significance was evaluated using two-way ANOVA with Sidak's multiple comparisons test. **h**, TCRα diversity between paired tissues ($n = 5$ biological replicates). Statistical significance was evaluated with one-way ANOVA followed by the Tukey's multiple comparison test. **i**, Heatmap illustrating the compositional TCRα similarity between paired samples assessed using the Morisita–Horn index. **j**, Bar graph indicates the relative abundance of TCRα clonotypes between patients with AF and patients in SR ($n = 5$ biological replicates). Data are presented as mean values ± s.d. Statistical significance was evaluated using two-way ANOVA with Sidak's multiple comparisons test. **k**, TCRα diversity between patients with AF and patients in SR ($n = 5$ biological replicates). Statistical significance was evaluated using the two-tailed Mann–Whitney *U*-test for non-parametric data and represented as mean ± s.d. Panels **h**–**k** show medians, and light dotted lines show 1st and 3rd quartiles. inf, infinity.

CCR7, *SELL* and *TCF7* (cluster 3); a cluster representing regulatory T cells (Tregs) expressing *FOXP3* and *CTLA4* (cluster 5); and a T follicular helper cell (Tfh) cluster characterized by the expression of *CXCL13*, *TOX2*, *CXCR5* and *PDCD1* (cluster 14). $CD8^+$ T cells comprised four clusters that included the following: three T_{RM} clusters expressing *CCL5*, the T_{RM} markers *CD69*, *PDCD1* and *CXCR6* and the cytotoxic-associated genes *GZMK* and *GZMA* (clusters 2, 8 and 9); and naive or T_{CM} cells expressing *CCR7*, *SELL* and *TCF7* (cluster 15). A small double-negative T cell cluster was identified by the expression of *CD3D* and absence of *CD4* and *CD8A* expression (cluster 18). In addition, we identified five B cell clusters based on the expression of *CD19*, *CD22* and *MS4A1*, with memory B cells expressing *CD27* and naive B cells expressing *IGHD*; high expression of *CD38* and *MZB1* defined a cluster of plasma B cells. A single cluster of monocytes/macrophages was identified based on the expression of *C5AR1*, *LYZ* and *CD14*, and a natural killer (NK) cell cluster was defined by the expression of *NCAM1*. Two clusters were found to be enriched in mitochondrial and heat shock protein genes indicative of a stress-like state and were integrated by a mixed population of monocytes and T cells. Expression of surface markers detected by TotalSeq antibodies (oligonucleotide-tagged antibodies) confirmed the expression of CD45RO on memory T cells as well as PD1 and CD69 expression on T_{RM} cells, which were also low on CCR7 (Extended Data Fig. 3b,c).

Consistent with our flow cytometry data, T_{RM} cells made up a sizeable proportion of the T cell repertoire, in particular for $CD8^+$ T cell populations. As expected, they differentially express genes associated with tissue retention/egress, but they lack expression of CD103, which is normally expressed on $CD8^+$ T_{RM} cells at the epithelial barrier[23] (Fig. 2c,d). T_{RM} cells exhibit constitutively high expression of deployment-ready mRNAs encoding effector molecules, such as granzymes, cytokines and chemokines, enabling rapid immune responses (Fig. 2d). Thus, to control their undue activation, they express the inhibitory molecules *LAG3* and *PDCD1* but lack the expression of *CTLA4* (ref. 20). Thus, CITE-seq provided the necessary single-cell resolution to demonstrate a gene signature consistent with that observed in other organs, such as the lung, gut and skin[24], and demonstrated that the elevated $CD69^+PD1^+$ T cell population observed in patients with AF is consistent with a T_{RM} cell phenotype with high effector cytotoxic function.

T_{RM} cells are recruited into the atrial myocardium

The EAT is now considered an immune site harboring an array of innate and adaptive immune cells and is thought to act as a reservoir for memory T cells[25]. Due to the absence of fascial boundaries and close functional and anatomic relationship, T cells present in the EAT could migrate and exert a detrimental effect on the myocardium. To characterize the T_{RM} cell populations between tissues, we identified differentially expressed genes (DEGs) for all T_{RM} cell clusters (Supplementary Table 4). Supporting the strong immune crosstalk between tissues, T_{RM} cells in EAT and AA showed a similar core phenotype. However, DEG analysis revealed an upregulation of activated genes—for example, *JUNB*, *FOS*, *ZFP36* and *IFNG*—in the T_{RM} cells present in the AA (Fig. 3a)[26], which could be confirmed by increased degranulation of $CD8^+$ T_{RM} cells (Fig. 3b). This activated phenotype was not restricted to T_{RM} cells but observed across immune cell clusters (Supplementary Table 4).

To further evaluate the dynamic relationship of T cells among EAT and AA tissues, CITE-seq was combined with TCR α-chain and β-chain sequencing. Distinct clonotypes were assigned according to the presence of unique nucleotide sequences for both α and β chains. A distinct pattern of T cell clonal expansion could be observed, with T_{RM} cells showing the highest degree of clonal expansion, in particular $CD8^+$ T_{RM} cells (Fig. 3c,d and Supplementary Table 5). STARTRAC-migr analysis revealed that T_{RM} cells are associated with the highest mobility with a high degree of TCR sharing between EAT and AA (Fig. 3e)[27]. TCR similarity was confirmed with the Morisita index (Extended Data Fig. 3d). To understand the trajectory of these cells, we performed DEG analysis on shared expanded clones between EAT and AA. Shared expanded TCR clones in the AA upregulate expression of *JUNB*, *FOS*, *IFNG*, *TNF* and *ZFP36* compared to EAT, which is consistent with T cell activation (Fig. 3f and Supplementary Table 6).

To confirm these findings, bulk TCRα-β sequencing was performed on matched blood, EAT and AA samples from six participants. Greater clonal expansion and lower clonotype diversity were detected in EAT and AA samples compared to blood (Fig. 3g,h and Extended Data Fig. 3e,f). In addition, a high degree of TCR similarity could be detected between EAT and AA paired samples, whereas a relative low proportion of shared TCR clonotypes was observed between tissues and blood (Fig. 3i), which is consistent with the tissue residency properties of T_{RM} cells. We then looked at T cell expansion in the EAT between patients with AF and patients in SR. Supporting the observed T_{RM} cell enrichment in patients with AF, clonal expansion was greater in the EAT of patients with AF compared to patients in SR, and diversity was reduced (Fig. 3j,k and Extended Data Fig. 3h,i). Together, these data support the notion that EAT acts as a reservoir of T_{RM} cells, which, upon activation, can migrate to the underlying myocardium to exert their function.

$CD8^{+/-}$ T_{RM} cells are transcriptionally diverse

Unsupervised clustering of CITE-seq data revealed a heterogeneous $CD8^+$ T_{RM} cell population. To further characterize the $CD8^+$ T_{RM} cells, DEGs between the three clusters were analyzed. Most of the DEGs were detected in cluster 9 compared to clusters 2 and 8, with clusters 2 and 8 differing only in the level of expression of effector molecules, such as

https://doi.org/10.1038/s44161-024-00532-x

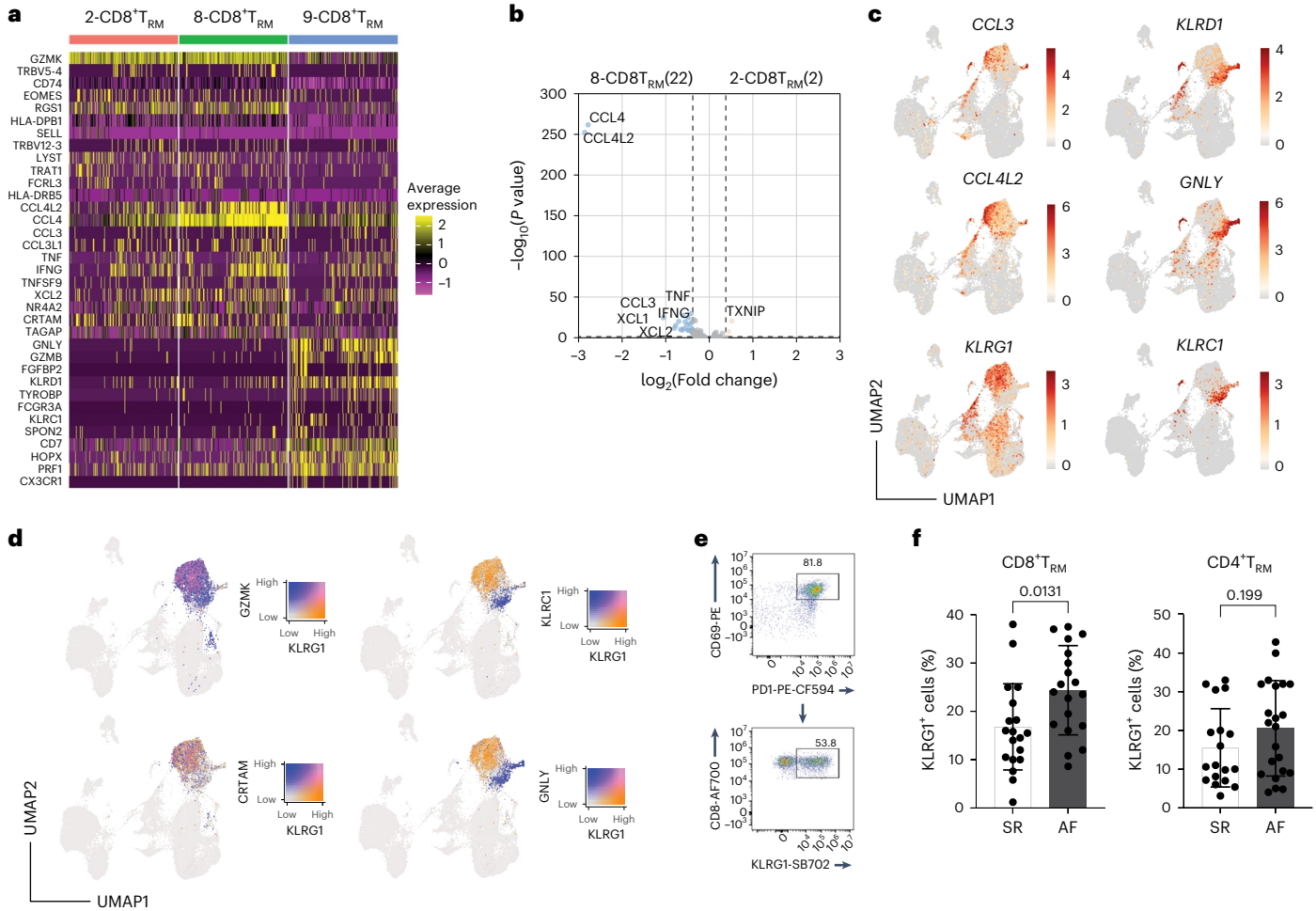

Fig. 4 | CITE-seq identifies two CD8$^+$ T_{RM} cell populations with a distinct core set of genes. a, Heatmap shows average gene expression by curated CD8$^+$ T_{RM} cell populations that had a fold change greater than 2 and $P < 0.05$ by the binomial test for at least one of the clusters. **b**, Volcano plots showing the average log fold changes and average Benjamini–Hochberg-corrected P values for pairwise differential expression between CD8$^+$ T_{RM} cell clusters 8 and 2 based on the non-parametric Wilcoxon rank-sum test. **c**, UMAP of representative selected genes differentially expressed between two main CD8$^+$ T_{RM} cell clusters. Color bars indicate average expression. Expression values are normalized for quantitative comparison within each dataset. **d**, UMAP showing co-expression of selective genes differentially expressed between two main CD8$^+$ T_{RM} cell clusters. Color bars indicate level of overlap expression. **e**, Representative dot plot showing KLRG1 expression. **f**, Bar graphs indicate the frequency of KLRG1$^+$CD4$^+$ and CD8$^+$ T_{RM} cells in the EAT. Each point represents an individual patient ($n = 22$ SR and $n = 18$ AF). Statistical significance was determined using two-tailed unpaired t-test for the parametrically distributed groups. Data are represented as mean and s.d.

CCL4, *CCL3* and *IFNG* (Fig. 4a,b and Supplementary Tables 7 and 8). Based on this, we concluded that clusters 2 and 8 are phenotypically similar populations in a different activation state. In contrary, cluster 9 appears to comprise a distinct CD8$^+$ T_{RM} cell population with differential expression of NK receptors and cytotoxic molecules (Fig. 4a and Supplementary Table 7). Two similar populations were described in human intestinal tissue, which could be differentiated by the expression of KLRG1 (refs. 28,29). With clusters 2 and 8 exhibiting a more cytotoxic/activated phenotype, we then investigated if these CD8$^+$ T_{RM} subsets were modulated in AF. We selected KLRG1 expression to assess CD8$^+$ T_{RM} heterogeneity, as this marker is more highly expressed in clusters 2 and 8 (Fig. 2d); shows little overlap with genes expressed in cluster 9 (Fig. 4d); and can easily distinguish two populations by flow cytometry (Fig. 4e). We found that KLRG1$^+$CD8$^+$ T_{RM} cells were elevated in the EAT of patients with AF compared to patients in SR (Fig. 4f). Although a causal relationship cannot be established, these results suggest that an increase in KLRG1$^+$CD8$^+$ T_{RM} cells could signal local atrial inflammatory activation in patients with AF.

Regional tissue remodeling in the EAT

AF is characterized by structural remodeling of the atrial myocardium, which generally involves fibrotic changes in the atria[30]. EAT has been proposed as an important factor involved in structural and electrical remodeling, with recent work showing morphological changes in the EAT/atrial border zone[31,32]. Clusters of inflammatory cells were identified in the transition zone between adipocytes and fibrosis in the human atrium, with T cells being the dominant cell type[33]. The presence of tertiary lymphoid structures was not evident in our cohort (Extended Data Fig. 4a,b). To examine biological changes and regionality dictating structural remodeling in AF, we performed NanoString GeoMx Digital Spatial Profiling (DSP) of tissue biopsies from two patients with AF and two patients in SR. The list of genes tested is shown in Supplementary Table 9. For this regional transcriptional analysis, samples from deep in the tissue and at the EAT/AA border zone were used as shown in Extended Data Fig. 4c,d. To identify regional differences between the EAT and atrial tissue, we performed DEG analysis between regions from the same tissue. As expected, t-distributed stochastic neighbor embedding (t-SNE) and principal component analysis (PCA) showed a distinct transcriptomic profile between the tissues (Extended Data Fig. 4e). In total, 780 genes were found to be differentially expressed between deep in the EAT compared to the border zone, with 813 genes found to be differentially expressed within regions in the atrium (Supplementary Tables 10 and 11). Volcano plots showing all the DEGs are

https://doi.org/10.1038/s44161-024-00532-x

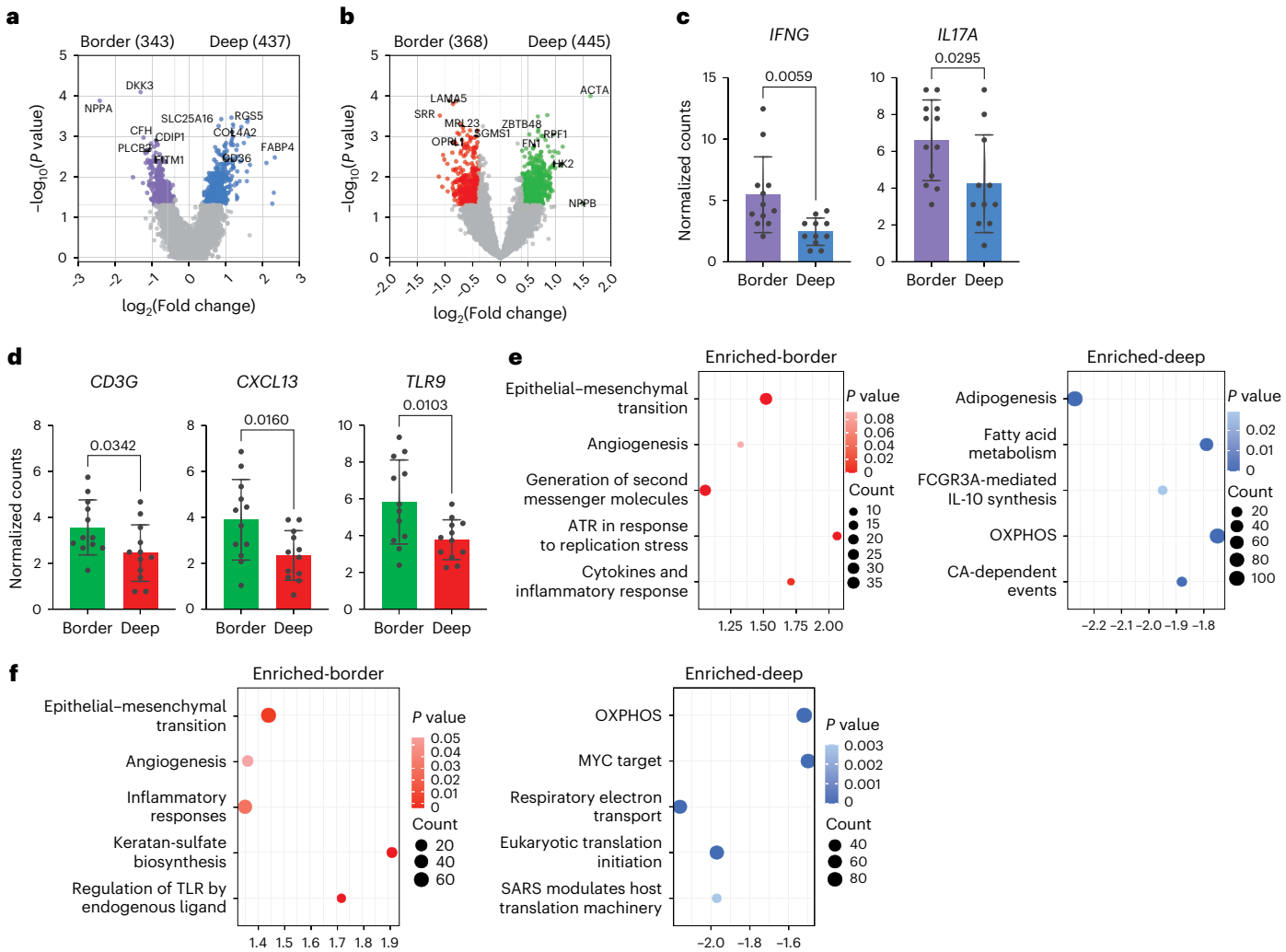

Fig. 5 | Regional differences identified by spatial transcriptomics. a, Volcano plot showing the average log fold changes in gene expression between border zone regions and deep in the tissue in the EAT. **b**, Volcano plot showing the average log fold changes in gene expression between border zone regions and deep in the tissue in the AA. **a**,**b**, Differential expression was performed using the linear mixed-effect model showing the average log fold changes and *P* values. **c**,**d**, Bar graph showing normalized counts of selective genes in the EAT (**c**) and AA (**d**), respectively. Statistical significance was determined using two-tailed paired *t*-test for parametric data, represented as mean and s.d. For normalized counts, Q3 normalization uses the top 25% of expressers to normalize across ROIs/segments **e**, GSEA pathway enrichment analysis of upregulated and downregulated DEGs in the EAT border zone compared to deep in the tissue. **f**, As in **e** but upregulated and dowregulated DEGs in the AA border zone compared to deep in the tissue. Pathway statistical significance was assessed using one-sided Fisher's exact test. **a**–**e**, Assays were performed in three biological replicates in technical triplicates.

shown in Fig. 5a,b. Genes associated with inflammation, including *IFNG* and *IL17A*, were upregulated in the border zone of the EAT (Fig. 5c), whereas *CD3G* was found to be upregulated in the atrium border zone as well as *CXCL13* and several Toll-like receptors (Fig. 5d). Pathway analysis identified upregulation of the epithelial–mesenchymal transition, angiogenesis and inflammation pathways in both EAT and cardiomyocyte border zone (Fig. 5e,f). A decrease in oxidative phosphorylation (OXPHOS) was detected in the EAT and AA border zone. A decline in mitochondrial OXPHOS activity was previously reported in chronic heart failure[34].

To investigate tissue remodeling, we performed a cellular deconvolution analysis. Cellular composition differs among tissues, with myeloid, lymphoid and mesothelial cells and fibroblasts being enriched in the EAT. As expected, adipocytes and atrial cardiomyocytes were exclusively present in the EAT and AA, respectively (Fig. 6a,b). Similarly, mesothelial cells were elevated in the EAT, probably due to the mesothelial lining of the heart. The EAT hosts the cardiac autonomic nerve fibers, the ganglionated plexi and a considerable amount of endothelial progenitor cells, explaining the elevated proportion of endothelial and neuronal cells (Fig. 6a,b). Consistent with the recognition of the adipose tissue as an immunological organ[35], a proportion of monocytes and lymphocytes was elevated in the EAT. This was confirmed by flow cytometry (Extended Data Fig. 4f). When investigating regional intra-tissue differences, fibroblasts were more abundant in the EAT border zone, whereas adipocytes were increased deep in the tissue, which supports previous reports on decreased adipogenesis in the border zone[31] (Fig. 6c). No differences were observed within the AA (Extended Data Fig. 4g).

We then investigated differences between the border zone of patients with AF and SR controls. Cellular deconvolution analysis showed a trend toward an increase in smooth muscle cells in the EAT of patients with AF, albeit not significant ($P = 0.06$) (Extended Data Fig. 3f,g). However, DEG analysis identified 700 and 380 genes being upregulated in the EAT and AA of patients with AF, respectively (Supplementary Tables 12 and 13). In addition, both EAT and AA showed upregulated fibrosis-related genes in patients with AF compared to SR controls (Fig. 6d,e). Similarly, inflammatory markers were upregulated in patients with AF (Fig. 6f,g). CCL5, which is highly expressed

https://doi.org/10.1038/s44161-024-00532-x

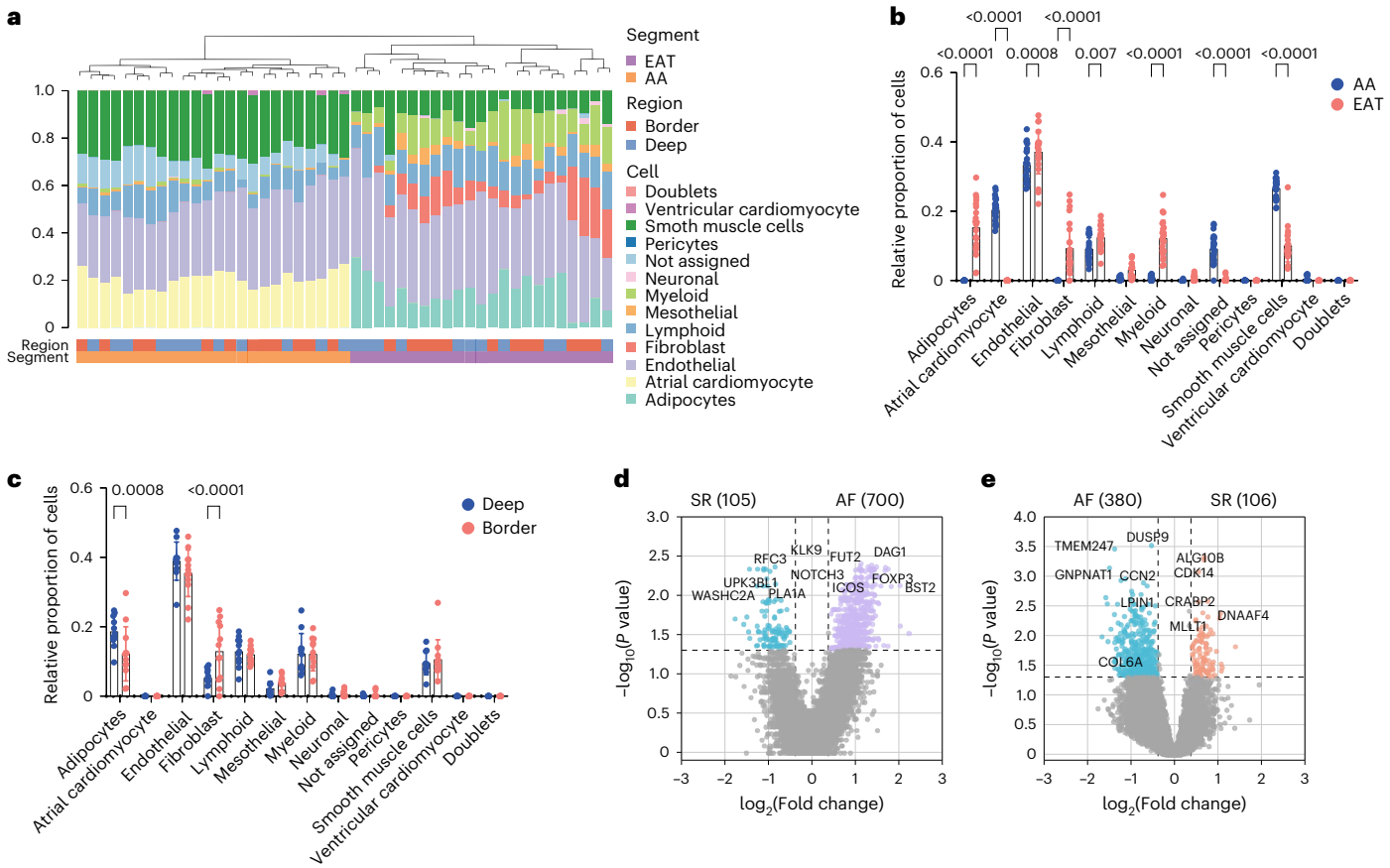

Fig. 6 | Tissue remodeling in the border zone. a, Proportion of cell types in the EAT and AA identified by cellular deconvolution. Each bar represents an individual ROI. **b**, Bar graph comparing the proportion of cell types over total cells between the EAT and AA. **c**, Bar graph comparing the proportion of cell types over total cells between the EAT border zone and deep in the tissue. **b**,**c**, Statistical significance was evaluated by two-way ANOVA with Sidak's multiple comparison test. Bars represent mean ± s.d. **d**, Volcano plots showing the average log fold changes in gene expression in the EAT border zone between patients with AF and patients in SR. **e**, As in **d** but showing expression differences in the AA border zone between patients with AF and patients in SR. **d**,**e**, Differential expression was performed using the linear mixed-effect model showing the average log fold changes and *P* values. **f**, Bar graph showing normalized counts of selective genes in the EAT border zone between patients with AF and patients in SR. **g**, As in **f** but in the AA border zone between patients with AF and patients in SR. **f**,**g**, Statistical significance was determined using two-tailed paired *t*-test for parametric data, represented as mean and s.d. For normalized counts, Q3 normalization uses the top 25% of expressers to normalize across ROIs/segments. **a**–**g**, Assays were performed in three biological replicates in technical triplicates.

by T_{RM} cells, was upregulated in the AA border zone in AF (Fig. 6g and Extended Data Fig. 3h). Together, these data indicate that the inflammatory response in the intersection within tissues is accompanied by secretion of pro-fibrotic factors and cellular remodeling at least in the EAT, which is more evident in patients with AF.

T_{RM} cells can directly modulate cardiomyocyte function

To evaluate the hypothesis that T_{RM} cells can significantly alter the electrical properties of coupled cardiomyocytes compared to non-T_{RM} cells, we performed co-culture studies with induced pluripotent stem cell–derived cardiomyocytes (iPSC-CMs) with an atrial phenotype. Atrial cardiomyocytes were differentiated as described by Cyganek et al.[36]. Contracting cardiomyocytes could be visualized around day 8 after differentiation, with spontaneous and consistent beating cell sheets evident after further maturation (Extended Data Fig. 5a–c). The cardiomyocyte phenotype was confirmed by transcriptomic, proteomic and electrophysiological analysis (Extended Data Fig. 5). Calcium is a fundamental link between the electrical activity in the heart and contractility of the cardiomyocytes. Changes in the calcium transient occur dynamically throughout the course of cardiomyocyte contraction, whereas perturbations in calcium flux are associated with arrhythmia vulnerability[37]. Co-culture of iPSC-CMs with $CD4^+$ T_{RM} cells isolated from EAT significantly altered calcium transient parameters at 50% (CaT_{50}) and 90% (CaT_{90}) decay in cellular

https://doi.org/10.1038/s44161-024-00532-x

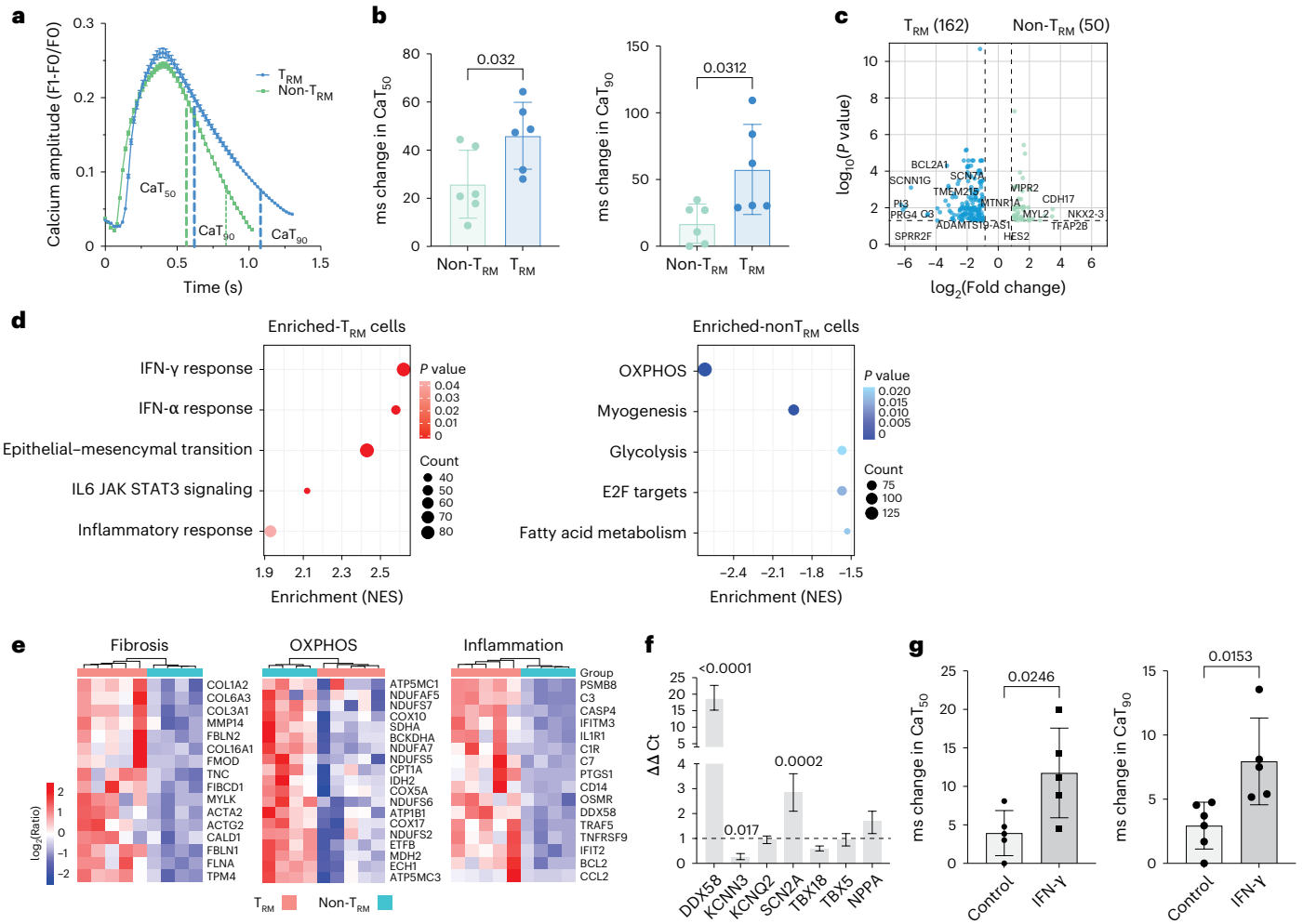

Fig. 7 | Calcium dynamics in iPSC atrial cardiomyocytes. a, Graph demonstrating a typical calcium transient after addition of T cells with the key parameters CaT_{50} and CaT_{90} depicted ($n = 6$ biological replicates). Each point represents mean ± s.e.m. **b**, Bar graphs demonstrating percentage change in CaT_{50} and CaT_{90} in $CD4^+$ T_{RM} and non-T_{RM} cells ($n = 6$ biological replicates). Statistical significance was assessed using two-tailed *t*-test for parametric data, represented as mean and s.d. **c**, Volcano plot demonstrating differential gene expression between the T_{RM} and non-T_{RM} samples. Significance threshold of $P < 0.05$ $\log_{10}$ adjusted and $\log_2$ fold change > 1. **d**, GSEA pathway enrichment analysis of upregulated and downregulated DEGs in the iPSC-CMs cultured with $CD4^+$ T_{RM} cells compared to non-T_{RM} cell cultures. Pathway statistical significance was assessed using one-sided Fisher's exact test. **e**, Heatmap showing expression of genes associated with fibrosis, OXPHOS and inflammation. **c**,**e**, The Wald test from the DESeq2 package was used to test significance using false discovery rate-adjusted *P* values. **f**, iPSC-CMs were cultured with recombinant 50 ng ml^{-1} IFN-γ for 8 h. Relative expression levels of selective genes in iPSC-CMs ($n = 6$ technical replicates from three independent experiments) were analysed by RT–PCR. Expression levels were normalized to GAPDH expression. Bars represent expression in treated cells compared to untreated, which was set at 1 and indicated with dotted lines. Bars represent the mean ratio and upper and lower limits. Statistical significance was determined using unpaired two-tailed *t*-test. **g**, Bar graphs demonstrating percentage change in CaT_{50} and CaT_{90} in iPSC-CMs treated with IFN-γ ($n = 5$ technical replicates). Statistical significance was determined using unpaired two-tailed *t*-test for parametric data, represented as mean and s.d. NES, normalized enrichment score.

calcium handling compared to co-cultures with non-T_{RM} memory $CD4^+$ T cells (Fig. 7a,b). The low frequency of non-T_{RM} memory $CD8^+$ T cells precluded collection of sufficient cells to assay their effects on cardiomyocyte calcium handling. However, similar changes in calcium flux were observed with total $CD8^+$ T cells (Extended Data Fig. 5d).

To determine whether transcriptomic alterations accompanied changes observed in calcium handling, we performed RNA-seq analysis of iPSC-CMs isolated after co-cultures. DEG analysis revealed an upregulation of gene-encoding ion channels—for example, *SCNN1*, *SCN7A*, *SCN2A*, *KCNQ2* and *KCNN3*—in iPSC-CMs co-cultured with $CD4^+T_{RM}$ cells compared to non-T_{RM} cells, with *KCNN3* and *SCN2A* previously associated with AF[38,39] (Fig. 7c and Supplementary Table 14). Interestingly, several extracellular matrix and collagen genes were upregulated in T_{RM} cell co-cultures, including *HAS1*, *PAPLN*, *FMOD*, *COL3A1*, *COL6A3* and *COL1A2*. Similar collagen expression was reported in iPSC-CMs under fibrotic stiffness[40]. Genes associated with apoptosis, such as *CASP4* and *BCL2*, and complement activation, for example, *C3*, *C7* and *C1R*, were also upregulatef on iPSC-CM-T_{RM} co-cultures. Gene set enrichment analysis (GSEA) identified an enrichment of genes associated with epithelial–mesenchymal transition and angiogenesis in T_{RM} cell co-cultures, and OXPHOS, adipogenesis and fatty acid metabolism were upregulated in iPSC-CMs co-cultured with non-T_{RM} memory $CD4^+$ T cells, which is consistent with regional differences detected with spatial transcriptomic analysis (Fig. 7d,e and Supplementary Table 14). Inflammatory pathways, such IFNs and inflammatory responses, were upregulated in iPSC-CM-T_{RM} co-cultures. This is likely a response to the enhanced production of pro-inflammatory cytokines and cytotoxic factors by T_{RM} cells (Fig. 7d). To test if cytokines alone could modulate iPSC-CMs, we analyzed selective gene expression changes in co-cultures performed in the presence of a 0.4-µm transwell.

Expression of genes, such as *NPPA* and *KCNN3*, was modulated by T_{RM} in both conditions, albeit at a higher level with direct cell-to-cell contact, whereas *KCNQ2* expression was upregulated only by direct contact (Extended Data Fig. 5e). *IFNG* expression is upregulated in the atria of patients with AF, and plasma IFN-γ has been described as an independent risk factor for all-cause mortality in AF[41,42]. IFN-γ is highly produced by T_{RM} cells, and its signaling pathway was upregulated in cardiomyocyte co-cultures. Thus, we then tested if IFN-γ alone could modulate iPSC-CM function. IFN-γ upregulates *DDX58* expression, consistent with the upregulation of the IFN-γ pathway, and was sufficient to modulate ion channel expression, such as *KCNN3* and *SCN2A*, and cellular calcium handling compared to untreated cells (Fig. 7f,g). IFN-γ production by T cells has been shown to modulate cardiomyocyte and cardiac fibroblast gene expression[43]. Indeed, IFN-γ stimulation of cardiac fibroblasts upregulated the expression of DDR2 and collagen genes (Extended Data Fig. 5f). Overall, our data suggest that T_{RM} cells can promote AF by several mechanisms.

Discussion

EAT has emerged as a risk factor and independent predictor of AF incidence and recurrence after ablation[44]. Inflammation has been described as a possible mechanism driving this increased risk. However, in-depth investigations of EAT immune profiling remain sparse. We and others have shown that EAT is highly enriched in adaptive immune cells, in particular T cells[19,45]. In the present study, we found that T_{RM} cells, which comprise a distinct subset of memory T cells in tissue, were significantly elevated in the EAT of patients with AF. These cells showed a high degree of expansion and migration toward the atrial tissue and can directly impair cardiomyocyte calcium handling. Furthermore, a highly heterogenous spatial organization is present within atrial border zones, implying a mechanism by which EAT may cause the non-uniform conduction disturbances observed in human AF.

T_{RM} cells have superior effector functions, including rapid chemokine/cytokine production and cytotoxicity[20], providing local protective immune responses against pathogens. More recently, however, it was demonstrated that T_{RM} cells can mediate autoimmunity, for example in inflammatory skin conditions, arthritis and Crohn's disease[29,46,47]. The role of T_{RM} cells in cardiovascular diseases, in particular AF, has not been explored. Here we demonstrated that the presence of T_{RM} cells positively correlates with production of IL-17 and IFN-γ, both known to be implicated in AF risk[48]. Furthermore, CITE-seq analysis identified heterogeneity within the $CD8^+$ T_{RM} cell pool. KLRG1 expression was used to define two main $CD8^+$ T_{RM} populations with distinct effector functions. Interestingly, these two subsets closely resemble the ones described in the context of intestinal inflammation[28,49], with $KLRG1^+$ T_{RM} cells identified by gene expression of *GZMK*, *GZMH*, *CCL4*, *CRTAM* and *KLRG1*, and a second population expressing CD103 was positive for *CD7*, *KLRB1* and *CAPG* expression, among others[49]. Of note, CD103 expression is limited to $CD8^+$ T_{RM} cells at mucosal sites and, therefore, was not expressed in T_{RM} cells in the EAT and AA[24]. Although $CD103^+$ T_{RM} cell frequency has been noted in healthy intestines, $KLRG1^+$ T_{RM} cells showing enhanced cytotoxic and proliferative potential were elevated in Crohn's disease[29]. These findings were later confirmed in a mouse model of intestinal infection[50]. In this model, CD103 fate mapping identified $CD103^-$ intestinal T_{RM} cells as the first responders to secondary infection. These cells were more frequently in contact with $CD11c^+$ dendritic cells in tissue and exhibited in situ proliferation, enhanced reactivation and effector function potential[50]. The association of KLRG1 expression with T_{RM} cell pro-inflammatory phenotype is particularly relevant given that the proportion of $KLRG1^+CD8^+$ T_{RM} cells was higher in patients with AF. Additional work is required to establish a direct link between the presence of $KLRG1^+CD8^+$ T_{RM} cells in the tissue and AF pathogenesis, but $KLRG1^+$ T_{RM} cells have the potential to serve as a predictive biomarker of disease persistence and/or recurrence.

It is worth noting the constitutive high expression of PD1 on T_{RM} cells[51,52]. PD1 is an inhibitory receptor, with its expression traditionally associated with T cell exhaustion. However, recent findings point toward an involvement of PD1 in restraining T_{RM} cell activation and immunopathology. Indeed, chronic pancreatitis is associated with reduced PD1 expression, and inhibition of the PD1/PDL1 axis resulted in enhanced T_{RM} cell-mediated functional responses[51]. Consistently, the presence of $PD1^+$ T_{RM} cells in tumors is associated with good prognosis and increased T cell effector capacity after anti-PD1/PDL1 immune checkpoint inhibitor (ICI) treatment[53,54]. However, PD1 blockade can also lead to cardiac arrhythmias in patients with cancer[49,55]. Moreover, the frequency of active episodes in patients with AF correlates with lower surface expression of PD1/PDL1 on peripheral $CD4^+$ T and dendritic cells[56]. Further investigation is required to understand the risk factors and to establish a link between T_{RM} cell activation and ICI-associated arrhythmias in these individuals.

EAT acts as a rich local depot of vasoactive molecules, cytokines and growth factors that can act on the heart or be secreted via the vaso vasorum into the coronary vessels (which supply both the EAT and myocardium) to exert its effects[12]. The EAT secretome varies considerably in physiological and pathophysiological states, with numerous lines of evidence implicating EAT inflammation as a key player in AF pathogenesis[12,16]. The EAT secretome applied to ex vivo atrial explants was found to induce fibrosis, a hallmark of AF, with transformation of fibroblasts into myofibroblasts and the production of a large amount of extracellular matrix components[57]. In vitro cultures with cardiomyocytes resulted in electrophysiological changes and electrical remodeling of cardiomyocytes[58]. Less is known about the direct role of immune cells and immune cell migration between tissues. Adipose tissue is increasingly recognized as an accessory immune organ contributing to immune responses. Fat-associated lymphoid clusters (FALCs) have been identified in several adipose tissue depots in mice and humans, which are not encapsulated organs, akin to tertiary lymph nodes supporting B cell responses[59]. In mice, adipose tissue has been shown to represent a memory T cell reservoir that provides rapid effector memory (EM) responses. These T cells were predominantly T_{RM} cells that expanded in situ and were redeployed to adjacent tissues to confer protection against secondary infections[25]. Our flow cytometry and spatial transcriptomic data support this idea that EAT is an immune reservoir where myeloid and lymphoid cells are present at higher numbers than in the heart tissue. This numeric advantage can be the result of a bioenergetic rich environment provided by the EAT and/or protective mechanism to restrain the accumulation of adaptive immune cells in the heart.

EAT/AA has emerged as a hotspot of fibrosis and cellular infiltration with large amounts of collagen deposition[31,32]. Due to the anatomical contiguity between EAT and AA, EAT may be a key driver of the fibrotic milieu, as evidenced by the accumulation of fibroblasts and upregulation of inflammatory and extracellular matrix components in the EAT border zone, which was exacerbated in patients with AF. The absence of cellular differences within the AA was surprising, in particular the low proportion of fibroblasts compared to EAT. Notably, many key highly expressed genes are shared between the collagen-producing myofibroblast population and smooth muscle cells, such as *MYH11* and *ACTA2*, suggesting that these cells may have not been adequately distinguished by the deconvolution algorithm. In addition, the deconvolution analysis did not allow for the identification of lymphoid cell subsets. The regional differences could be explained, at least in part, by inter-tissue and intra-tissue T_{RM} cell migration, supported by the dynamic relationship observed among T_{RM} TCR clones. T cell expansion was predominately detected among T_{RM} cells showing a high degree of shared clonality, highlighting the local immune crosstalk between the overlying adipose tissue (EAT) and the myocardium (AA). The finding that T_{RM} cells in general, and TCR-expanded clones in particular, have a more activated phenotype in the AA compared to EAT suggests a

migration process from the reservoir in the EAT toward the effector site in the AA. Similar findings have recently been described in the context of heart failure[60]. High shared clonality could be detected between the EAT and the heart, with T cells having a more activated phenotype in these patients. This is no surprise given that AF and heart failure have common pathophysiological mechanisms[61], with EAT dysfunction and inflammation thought to play an instrumental role in both disease processes.

Relative to patients in SR, the number of T cells has been shown to be elevated in the atrial tissue of patients with AF[62], with an early study highlighting an accumulation of $CD8^+$ T cells at the EAT/AA tissue border zone[33]. However, how T cells can directly impair atrial conduction and function is not established. T cells are key mediators of tissue inflammation, which can alter atrial electrophysiology. Inflammatory cytokines, such as TNFα, IL-1β and IL-17, can markedly enhance the risk of arrhythmic events by directly promoting electrical and structural cardiac remodeling[48]. In addition, IFN-γ has been shown to exert a sustained inhibitory effect on cardiac L-type calcium channels[63] and to induce a metabolic shift in cardiomyocytes with downregulation of OXPHOS, which is consistent with the failing heart[43]. We showed that $CD4^+$ T_{RM} cells were able to uniquely alter the calcium handling properties of atrial cardiomyocytes by inducing electrical and structural changes as evidenced by gene expression changes in ion channels, calcium signaling, tracellular matrix and collagen. This is consistent with the high production of pro-inflammatory cytokines by T_{RM} cells—for example, TNF-α and IFN-γ—although a direct cell-to-cell contact, for example by NK receptor binding, cannot be ruled out. T_{RM} cells also express a cluster of chemokines and chemokine receptors, with CCL5 emerging as a possible mediator of tissue inflammation. CCL5 mediates trafficking and homing of T cells and innate cells to sites of inflammation. CCL5 is mainly expressed by T cells and monocytes, although CITE-seq analysis identified T_{RM} cells as the main producers of CCL5 in the EAT and AA, with $CCL5^+$ cells in the border zone showing a clear lymphocyte morphology. Blocking of CCL5 significantly reduced infarct size in mouse models of heart failure and was identified as a key inflammatory mediator in the EAT of patients with heart failure[60,64]. Furthermore, production of CCL5 by T_{RM} cells is thought to be responsible for arthritis flares by promoting the recruitment of T_{EM} cells to the joint[47].

An important limitation of this study is that, due to the nature of the tissue analyzed, samples were obtained from patients with heart conditions that may themselves alter the physiology of the EAT and AA. Although the presented data provide evidence of a strong association between T_{RM} cell-induced inflammation and increased susceptibility to AF, a causative relationship was only partially confirmed by in vitro iPSC cultures. A limitation of the iPSC-CM system is that T cell exposure to self-antigens that may be present in patients with AF is limited. In addition, it is likely that the effect of T_{RM} cells in cardiomyocytes was underestimated, as the outcome of a positive feedback loop effect—for example, recruitment of innate and adaptive immune cells to the site of inflammation—can be assessed only in the presence of a full immune system.

Methods

Study population and sample collection

All patients provided written informed consent for their participation in the study as per local research procedures and Good Clinical Practice guidance (Research Ethics Committee reference: 14/EE/0007). Adult (≥18 years) patients undergoing on-pump open chest coronary artery bypass grafting (CABG) surgery and/or valve reconstruction (VR) surgery were recruited from Barts Heart Centre, St. Bartholomew's Hospital, in London, United Kingdom (UK), via the Barts BioResource. Exclusion criteria included congenital heart disease; underlying cardiomyopathies or ion channelopathies; primarily undergoing other cardiac surgical procedures (for example, aortic surgery); off-pump CABG surgery; patients with active endocarditis, myocarditis or pericarditis; patients with pre-existing inflammatory diseases (for example, rheumatoid arthritis); active malignancy; patients on immunomodulatory or biologic drugs (for example, tacrolimus and anti-TNF-α agents); perioperative rhythm control therapies (for example, use of amiodarone); postoperative hemodynamic shock; uncorrected potassium derangement ($K < 3.3$ or $K > 5.8$); and uncorrected magnesium derangement ($Mg < 0.5$ or $Mg > 1.5$) detected on laboratory blood sample analysis. Fasting venous blood samples were collected preoperatively in the anesthetic room. Approximately 0.8–1 g of adipose tissue samples was collected in ice-cold PBS with 2% FBS. SAT was collected immediately after the median sternotomy incision, and EAT was obtained after opening up of the pericardial sac. AA tissue was obtained after insertion of the right atrial cannula as part of transitioning patients on to cardio-pulmonary bypass, and, typically, 0.1–0.5 g of AA tissue was harvested.

Sample processing

Adipose tissue samples were processed as previously described[65]. AA samples were enzymatically digested with 675 U collagenase I (Sigma-Aldrich), 187.5 U collagenase XI (Sigma-Aldrich) and 10 U DNase (Sigma-Aldrich) in 1 ml of HBSS modified with 10 mM HEPES but without phenol red (STEMCELL Technologies) per gram of tissue. The cell–enzyme suspension was incubated at 37 °C with 225-r.p.m. agitation for 45 min. Then, 5 ml of fasting venous blood samples was collected in EDTA tubes (BD Biosciences) preoperatively in the anesthetic room. Peripheral blood mononuclear cells (PBMCs) were isolated using Ficoll-Paque PLUS (Cytiva) as per the manufacturer's instructions. Single-cell suspensions were obtained after centrifugation and red cell lysing before antibody staining.

Flow cytometry

Immune cells from blood, adipose tissue and AA tissue were isolated as described previously. Immune cells were stained with fixable Aqua Live/Dead cell stain (Invitrogen) diluted 1:1,000 and fluorochrome-conjugated antibodies specific for CD197-FITC, CD19-PerCP-Cy5.5, CD45RO-BV421, CD335-BV605, CD45-BV785, CD127-APC, CD8-AF700, CD3-APC/Cy7, CD69-PE, CD4-PE/Cy7, PD1-PE-CF594, CD303-FITC, CD123-PerCP/Cy5.5, CD206-BV421, CD3-BV605, CD19-BV605, CD14-APC, CD16-AF700, CD1c-APC/Cy7, Clec9A-PE, CD1a-PE-CF594 and CD141-PE/Cy7 from BioLegend and KLRG1-SB702 from eBioscience. The samples were stained at 4 °C for 18 min and then washed twice with fluorescence-activated cell sorting (FACS) buffer where the plate was centrifuged at 400*g* for 3 min and the supernatant discarded. The samples were then fixed in stabilizing fixative buffer (BD Biosciences) containing 3% paraformaldehyde at 4 °C for 30 min.

For intracellular cytokine staining, samples were resuspended in 500 µl of Aim V medium with the addition of 1 µl of Cell Activation Cocktail (BioLegend). After 4-h incubation, samples were washed and stained for surface markers as detailed above, followed by permeabilization and fixation in the permeabilization/fixation buffer (BD Biosciences) at 4 °C for 12 min. Intracellular cytokine production was evaluated by incubation for 15 min at 4 °C with fluorochrome-conjugated antibodies specific for IFN-γ-APC, IL-17-APC/Cy7 and IL-22-PE (BioLegend). Data were acquired on a CytoFLEX (Beckman Coulter) and analyzed using FlowJo version 10 software.

CITE-seq and single-cell TCR sequencing

Paired AA and EAT samples were collected from two patients with AF (1× VR and 1× CABG) and digested as outlined above. The CITE-seq samples were prepared following the steps outlined in the 10x Genomics Cell Surface Protein Labeling for Single Cell RNA Sequencing protocols with the Feature Barcode technology protocol preparation guide (document CG000149). In brief, samples were resuspended in 50 µl of

PBS + 1% BSA and 5 µl of human TruStain FcX and incubated for 10 min at 4 °C. Fixable Aqua Live/Dead cell stain (Invitrogen) and CD45 PE antibodies (BioLegend) and TotalSeq antibodies were resuspended in PBS and added to the sample suspension to a create a total sample volume of 155 µl. The following TotalSeq antibodies (BioLegend) were employed: C0138 anti-human CD5, C0358 anti-human CD163, C0160 anti-human CD1c, C0049 anti-human CD3, C0072 anti-human CD4, C0080 anti-human CD8a, C0087 anti-human CD45RO, C0148 anti-human CD197, C0146 anti-human CD69, C0088 anti-human CD279 and C1046 anti-human CD88. Samples were then incubated at 4 °C for 30 min in the dark. After washing, samples were incubated for 15 min with MojoSort human anti-PE Nanobeads followed by magnetic purification as per the manufacturer's instructions (BioLegend) for $CD45^+$ enrichement. Live $CD45^+$ cells were further purified by FACS with an LSRFortessa analyzer (BD Biosciences).

The 10x Genomics CITE-seq

Chromium Next GEM Single Cell 5′ v2 (dual index) with Feature Barcode technology for Cell Surface Protein & Antigen Specificity User Guide (CG000330) was employed at the UCL Single-Cell Sequencing facility. In brief, the cell suspension was partitioned into a nanoliter-scale droplet emulsion using the 10x Genomics Chromium Single Cell Controller with RNA-seq libraires created using the Chromium Next GEM Single Cell 5′ Reagent Kits and a Gel Bead Kit v2. Gel beads in emulsion (GEM) were generated by combining the barcoded Single Cell VDL 5′ gel beads with a master mix containing the cell surface protein-labeled cells and partitioning oil onto a Chromium Next GEM chip. The gel beads were dissolved, and the cells were lysed. After reverse transcription, barcoded full-length cDNA was generated from the poly-adenylated mRNA. Silane magnetic beads (Dynabeads MyOne SILANE) were used to purify the 10x barcoded cDNA. Libraries were then sequenced in-house at the UCL Single-Cell Sequencing facility on an Illumina NextSeq 500/550 sequencing platform.

CITE-seq data processing

CITE-seq data processing was performed at the UCL City of London Centre Single-Cell Sequencing core. In brief, output from the Chromium Single Cell 5′ v2 sequencing was processed using Cell Ranger (version 6.0.1) analysis pipelines. FASTQ files were generated using Cell Ranger mkfastq (version 6.0.1). Gene expression reads were aligned to the human reference genome GRCh38 and counted using Cell Ranger count (version 6.01.) VDJ reads were aligned to the GRCh38 VDJ reference dataset using Cell Ranger vdj (version 6.01). 10x feature barcoding was performed using the antibodies outlined above, the reads for which were counted using Cell Ranger count.

Expression matrices were analyzed using the Seurat package (version 4.0.03) in R. Cells with mitochondrial reads making up more than 10% of the total read count, or with fewer than 400 genes detected, were removed. A multiplet filtering step using DoubletFinder (version 2.0.3) was performed using the author-recommended settings. Normalization was performed on the dataset using SCTransform (version 0.3.2) using centered log-ratio normalization and the top 3,000 variable genes. This was followed by Seurat (version 4.0.3) integration to remove batch effects, and the top 3,000 genes minus TCR genes were used as integration features. PCA and UMAP dimensionality reduction (dims 1:30) was performed using RunPCA and RunUMAP from the single-cell RNA-seq data only. Clustering was performed using the FindClusters function in the Seurat package using a resolution of 0.8. All differential gene expression analysis was carried out on log-normalized gene expression values using the Seurat NormalizeData function with default parameters through the MAST algorithm within FindMarkers. Feature barcoding reads were normalized using a centered log-ratio transformation. VDJ data were integrated using strict clone calling—matching VDJC gene and TRA/TRB nucleotide sequences. Analysis was performed using scRepertoire (version 1.3.5) and STARTRAC (version 0.1.0).

Bulk TCR sequencing

Bulk TCR α and β sequencing was performed from paired blood AA and EAT samples from five patients with AF. In addition, TCR sequencing was performed using additional EAT from five patients in SR. cDNA was extracted from tissues and whole blood. A quantitative experimental and computational TCR sequencing pipeline was employed as previously described[66]. The pipeline introduces unique molecular identifiers (UMIs) attached to individual cDNA TCR molecules, allowing correction for PCR and sequencing errors. TCR identification, error correction and CDR3 extraction were performed following a suite of tools available at https://github.com/innate2adaptive/Decombinator, as detailed in Peacock et al.[66]. TCR frequency and similarity were analyzed using the Immunarch package in R (version 1.0.0). The level of similarity between the different TCR repertoires was measured using the Morisita–Horn index, ranging from 0 (no similarity) to 1 (identical), which takes into account the shared sequences and clonal frequency between samples. Antigen matching analysis was performed via the McPAC-TCR database.

Spatial transcriptomics

Spatial profiling was carried out by NanoString Technologies using a GeoMx DSP. AA tissue with surrounding EAT samples was selected from four patients, of which two were from patients with AF and two were from patients in SR. The technology is based on the principle of in situ hybridization. After dewaxing of the formalin-fixed, paraffin-embedded (FFPE) slides, Tris-EDTA buffer was added to expose the RNA targets, and a proteinase K digestion was performed to remove any protein bound to RNA. The tissue was incubated overnight at 37 °C with GeoMx RNA detection probes. Labeled antibodies, FABP4 for adipocytes and troponin for cardiac tissue were added to image the tissue. The GeoMx DSP uses an automated microscope to image the tissue sections and cleave/collect the photocleavable indexing oligonucleotides. Specific regions of interest (ROIs) were then pre-selected on either side of the border zones of the AA/EAT and deep in the AA and deep in the EAT in triplicates. ROIs were quantified using RNA-seq technology on the Illumina platform to generate RNA expression data within a spatial context.

Spatial transcriptomics data processing

Data were analyzed with the GeoMx DSP Analysis Suite. The first quality control step looks at the 'raw read threshold' flagging segments with fewer than 1,000 raw reads. A second step assesses the percentage of aligned reads. The sequenced barcodes should match the known GeoMx library of barcodes; hence, a high percentage alignment should be expected (an alignment threshold value less than 80% is typically used to flag segments). Sequencing saturation was assessed as 1 − (aligned reads/de-duplicated reads). A value of less than 50% sequencing saturation was used to flag segments. A background quality control step was additionally performed based on negative probes. A no-template control was included in the first well of each collection plate with the negative control in PCR reading very low counts. The Grubbs outlier test is performed to exclude a probe from all segments if the probe is higher or lower in more than 20% of segments. A limit of quantitation value is also defined where a target is considered to be detected with high confidence, the default setting here being 2 standard deviations above the geometric mean of the negative probes. Filtering was performed to further refine the dataset, followed by Q3 normalization.

For spatial deconvolution, the SpatialDecon plugin in R version 1.2 (NanoString Technologies) was employed. The human heart benchmarking cell matrix used for the alignment of the GeoMx spatial gene expression data was extracted from the single cell data of the human heart (heartcellatlas.org). The deconvolution script with the adjusted cell matrix was run on the GeoMx DSP Analysis Suite applied to the normalized spatial gene expression data.

iPSC atrial cardiomyocyte and cardiac fibroblast differentiation

iPSC lines were acquired from the Human Induced Pluripotent Stem Cell Initiative (HipSci) deposited by the Wellcome Trust Sanger Institute into the Culture Collections archive (UK Health Security Agency). Each cell line was resuscitated as per the HipSci guidance (https://www.culturecollections.org.uk/media/109442/general-guidelines-for-handling-hipsci-ipscs.pdf) in TeSR-E8 media (STEMCELL Technologies). Plates were coated with a vitronectin coating (Thermo Fisher Scientific) to provide an appropiate adhesive surface for culturing iPSCs. Rho kinase (ROCK) inhibitor RevitaCell (Thermo Fisher Scientific) was added to TeSR-E8 medium to achieve a final concentration of 10 µM (1:1,000 dilution from the stock solution). Cells were plated in 2 ml of TeSR-E8 RevitaCell media per well in a six-well plate. iPSC media were replaced daily with fresh TeSR-E8. Cells were typically split at a ratio of 1:4 every 6–7 d, following HipSci guidance. iPSC-CM derivation was carried out as per Cygnaek et al.[36]. The base cardiomyocyte differentiation medium (CDM) used was RPMI 1640 with HEPES and GlutaMAX (Thermo Fisher Scientific) supplemented with 0.2 mg ml^{-1} ascorbic acid and 0.5 mg ml^{-1} albumin. Cells were sequentially treated with 4 µM CHIR99021 (Sigma-Aldrich) for 48 h, followed by 5 µM IWP2 (Sigma-Aldrich) for 48 h to induce a cardiac cell lineage. To drive differentiation toward an atrial cell phenotype, the cells were administered 1 µM retinoic acid at days 3–6. At day 6, simple CDM was added. Monolayers of beating iPSC-CMs were typically observed at days 7–8 onwards. The cells were maintained in RPMI 1640 + HEPES + GlutaMAX with the addition of 2% B27 supplement (Thermo Fisher Scientific).

For differentiation of cardiac fibroblasts, iPSCs were cultured in CDM with CHIR99021 for 1 d to induce a cardiac cell lineage as described above. After day 1, the medium was changed to CDM and cultured for an additional 24 h. After day 2, the medium was changed to a cardiac fibroblast-based medium (CFBM) comprising DMEM, 500 µg ml^{-1} albumin, 0.6 µM linoleic acid, 0.6 µg ml^{-1} lecithin, 50 µg ml^{-1} ascorbic acid, GlutaMAX, 1 µg ml^{-1} hydrocortisone hemisuccinate and 5 µg ml^{-1} insulin. CFBM was supplemented with 75 ng ml^{-1} bFGF, and media were replaced every other day until day 20 of differentiation.

iPSC atrial cardiomyocyte calcium imaging assays

The atrial cardiomyocytes were differentiated on a 48-well plate setup (Corning). Only wells where there was spontaneous and consistent beating of the cardiomyocytes across the well were imaged. The rate of spontaneous beating was not controlled, as this would require pacing the monolayer of the sheets. However, the percentage change in the decay time was calculated for each well before and after co-culture with T_{RM} and non-T_{RM} cells. Given that this was a percentage change for each well, taking into account the same cardiomyocyte well density and beating characteristics, different wells could be compared by determining the percentage change in decay time for each well.

For T_{RM} cell purification, cells were initially stained with fixable Aqua Live/Dead cell stain, CD45 PE, CD45RO, CD8-AF700, CD3-APC/Cy7, CD69-PE, CD4-PE/Cy7 and PD1-PE-CF594 as previously discussed. Samples were then incubated at 4 °C for 20 min in the dark, after which samples were incubated for 15 min with MojoSort human anti-PE Nanobeads, followed by magnetic purification as per the manufacturer's instructions (BioLegend) for $CD45^+$ enrichement. Live T_{RM} cells were purified by FACS (LSRFortessa analyzer) and $CD45RO^+CD69^+PD1^+$ cells. Non-T_{RM} cells were purified as $CD45RO^+CD69^-PD1^-$ cells. Cells were added to cardiomyocytes at 2×10^3 per well.

Calcium imaging was performed using the calcium indicator dye Fluo-4 AM (Invitrogen). Monolayers were illuminated with a single green light from a high-power LED with a center at wavelengths of 505 nm filtered with a bandpass excitation filter (490–510 nm). The LED power supply was custom built by Cairn Research. A Hamamatsu ORCA Flash 4.0 V2 camera was connected to a Nikon Eclipse TE200 inverted microscope, and a camera magnification objective of ×10 (numerical aperture 0.3) was used to provide a broad field of view. A bandpass emission filter (520–550 nm) was used to ensure that fluorescence emitted only after calcium indicator excitation was detected. HCImageLive (Hamamatsu) imaging software was used to acquire the data. The recording was then analyzed using custom in-house software (Queen Mary University of London). A total recording time of 20 s was used with a frame rate of 50 frames per second (image acquisition every 20 ms) to produce an image stack of 1,000 frames. Images were cropped to an area of 600 × 600 pixels that contained the projected image, and pixel binning was performed to improve signal-to-noise ratio. The recording was analyzed to drive a signal average calcium waveform from across the entire field of view. Relevant waveform statistics, including time to peak, time to 50% recovery to baseline (T_{50}) and time to 90% recovery to baseline (T_{90}), were determined. The data were exported as a CSV file for analysis in GraphPad Prism. Comparisons between different experimental conditions were, therefore, possible in a consistent and reproducible fashion, enabling assessment of how cardiomyocyte calcium flux changed before and after T_{RM} co-cultures.

iPSC co-culture RNA expression analysis

Cells were washed with PBS, and RNA was extracted with an RNeasy Micro Kit (Qiagen) following the manufacturer's instructions. Illumina sequencing was carried out at Novogene Bioinformatics Technology Co., Ltd. Raw FASTQ files were first trimmed using Trim Galore (version 0.6.7) and inspected for quality control using fastqc (version 0.11.9) and multiqc (version 1.12). Transcript and genome files were downloaded from GENCODE, release 43 (GRCh38.p13), to generate decoy index files with Salmon (version 1.10.1). Next, Salmon was used to perform transcript quantification with the additional parameter –gcbias. Salmon transcript quantifications were imported into R (version 4.1.0) to aggregate transcripts to genes using the package tximport (version 1.22.0). Genes with a read count of less than 5 were excluded from further analysis: rowSums(counts()) ≥ 5. Differential gene analysis was performed using DESeq2 (version 1.34.0). GSEA (version 4.3.2) was performed using normalized gene counts generated by DESeq2.

For RT–PCR, reverse transcription to cDNA was performed using High-Capacity RNA-to-cDNA kits (Applied Biosystems, Thermo Fisher Scientific). The relevant primer sequences can be found in Supplementary Table 15 (Thermo Fisher Scientific). Gene expression was performed using SYBR Green Supermix (Bio-Rad), as per the manufacturer's instructions, and analyzed using the Light Cycler System (Roche). Relative gene expression values were determined using the ΔΔCT method and normalized to a stable reference housekeeping gene control (GAPDH). The control values were set at 1. Given that the ΔΔCT method is not normally distributed, the geometric mean was used for the representation of the data.

Statistical analysis

Statistical significance was determined for continuous variables where two groups were assessed using two-tailed Student's *t*-test where the data were parametric and Mann–Whitney *U*-test for non-parametric data. The χ^2 test or Fisher's exact test was used for categorical data. Data were analyzed using GraphPad Prism version 8. Normality was assessed using the Kolmogorov–Smirnov and Shapiro–Wilk tests. Where parametric data are represented, the mean and standard deviation values are reported, and, for non-parametric data, median and interquartile ranges are reported. A *P* value of less than 0.05 was considered statistically significant.

Reporting summary

Further information on research design is available in the Nature Portfolio Reporting Summary linked to this article.

Data availability

CITE-seq and RNA-seq raw and processed data are deposited in the Gene Expression Omnibus (GEO) under accession number GSE263154. Cell Ranger version 6.0.1 was used with default parameters to map all the data from the samples to the human reference genome (GRCh38; https://www.ncbi.nlm.nih.gov/datasets/genome/GCF_000001405.26/). Bulk TCR sequencing data are available at Zenodo (https://doi.org/10.5281/zenodo.13318819) (ref. 67). The suite of tools for TCR sequencing analysis can be accessed at https://github.com/innate2adaptive/Decombinator. Spatial transcriptomic raw sequencing data have been deposited in the GEO under accession number GSE261363. Spatial profiling was carried out using the NanoString Technologies GeoMx Digital Spatial Profiler. iPSC-CM RNA-seq datasets have been deposited in the GEO under accession number GSE256520. Additional data generated in this study are provided in the Supplementary Information and Source Data sections.

References

1. Wijesurendra, R. S. & Casadei, B. Mechanisms of atrial fibrillation. *Heart* **105**, 1860–1867 (2019).
2. Wang, T. J. et al. Temporal relations of atrial fibrillation and congestive heart failure and their joint influence on mortality: the Framingham Heart Study. *Circulation* **107**, 2920–2925 (2003).
3. Wolf, P. A., Abbott, R. D. & Kannel, W. B. Atrial fibrillation as an independent risk factor for stroke: the Framingham Study. *Stroke* **22**, 983–988 (1991).
4. Burdett, P. & Lip, G. Y. H. Atrial fibrillation in the UK: predicting costs of an emerging epidemic recognizing and forecasting the cost drivers of atrial fibrillation-related costs. *Eur. Heart J. Qual. Care. Clin. Outcomes* **8**, 187–194 (2022).
5. Zhou, X. & Dudley, S. C. Evidence for inflammation as a driver of atrial fibrillation. *Front. Cardiovasc. Med.* **7**, 62 (2020).
6. Anderson, J. L. et al. Frequency of elevation of C-reactive protein in atrial fibrillation. *Am. J. Cardiol.* **94**, 1255–1259 (2004).
7. Marcus, G. M. et al. Interleukin-6 and atrial fibrillation in patients with coronary artery disease: data from the Heart and Soul Study. *Am. Heart J.* **155**, 303–309 (2008).
8. Chen, M. C. et al. Increased inflammatory cell infiltration in the atrial myocardium of patients with atrial fibrillation. *Am. J. Cardiol.* **102**, 861–865 (2008).
9. Yamashita, T. et al. Recruitment of immune cells across atrial endocardium in human atrial fibrillation. *Circ. J.* **74**, 262–270 (2010).
10. Qu, Y. C. et al. Activated nuclear factor-κB and increased tumor necrosis factor-α in atrial tissue of atrial fibrillation. *Scand. Cardiovasc. J.* **43**, 292–297 (2009).
11. Ihara, K. & Sasano, T. Role of inflammation in the pathogenesis of atrial fibrillation. *Front. Physiol.* **13**, 862164 (2022).
12. Mazurek, T. et al. Human epicardial adipose tissue is a source of inflammatory mediators. *Circulation* **108**, 2460–2466 (2003).
13. Vyas, V., Hunter, R. J., Longhi, M. P. & Finlay, M. C. Inflammation and adiposity: new frontiers in atrial fibrillation. *Europace* **22**, 1609–1618 (2020).
14. Nakamori, S., Nezafat, M., Ngo, L. H., Manning, W. J. & Nezafat, R. Left atrial epicardial fat volume is associated with atrial fibrillation: a prospective cardiovascular magnetic resonance 3D Dixon study. *J. Am. Heart Assoc.* **7**, e008232 (2018).
15. Yorgun, H. et al. Association of epicardial and peri-atrial adiposity with the presence and severity of non-valvular atrial fibrillation. *Int. J. Cardiovasc. Imaging* **31**, 649–657 (2015).
16. Mazurek, T. et al. Relation of proinflammatory activity of epicardial adipose tissue to the occurrence of atrial fibrillation. *Am. J. Cardiol.* **113**, 1505–1508 (2014).
17. Xie, B., Chen, B. X., Wu, J. Y., Liu, X. & Yang, M. F. Factors relevant to atrial ^{18}F-fluorodeoxyglucose uptake in atrial fibrillation. *J. Nucl. Cardiol.* **27**, 1501–1512 (2020).
18. Sanfilippo, A. J. et al. Atrial enlargement as a consequence of atrial fibrillation. A prospective echocardiographic study. *Circulation* **82**, 792–797 (1990).
19. Vyas, V. et al. Obesity and diabetes rather than coronary disease per se are major risk factors for epicardial adipose tissue inflammation. *JCI Insight* **6**, e145495 (2021).
20. Kumar, B. V. et al. Human tissue-resident memory T cells are defined by core transcriptional and functional signatures in lymphoid and mucosal sites. *Cell Rep.* **20**, 2921–2934 (2017).
21. Liu, Y., Ma, C. & Zhang, N. Tissue-specific control of tissue-resident memory T cells. *Crit. Rev. Immunol.* **38**, 79–103 (2018).
22. Stoeckius, M. et al. Simultaneous epitope and transcriptome measurement in single cells. *Nat. Methods* **14**, 865–868 (2017).
23. Barros, L., Ferreira, C. & Veldhoen, M. The fellowship of regulatory and tissue-resident memory cells. *Mucosal Immunol.* **15**, 64–73 (2022).
24. Szabo, P. A., Miron, M. & Farber, D. L. Location, location, location: tissue resident memory T cells in mice and humans. *Sci. Immunol.* **4**, eaas9673 (2019).
25. Han, S.-J. et al. White adipose tissue is a reservoir for memory T cells and promotes protective memory responses to infection. *Immunity* **47**, 1154–1168 (2017).
26. Jurgens, A. P., Popović, B. & Wolkers, M. C. T cells at work: how post-transcriptional mechanisms control T cell homeostasis and activation. *Eur. J. Immunol.* **51**, 2178–2187 (2021).
27. Zhang, L. et al. Lineage tracking reveals dynamic relationships of T cells in colorectal cancer. *Nature* **564**, 268–272 (2018).
28. FitzPatrick, M. E. B. et al. Human intestinal tissue-resident memory T cells comprise transcriptionally and functionally distinct subsets. *Cell Rep.* **34**, 108661 (2021).
29. Bottois, H. et al. KLRG1 and CD103 expressions define distinct intestinal tissue-resident memory CD8 T cell subsets modulated in Crohn's disease. *Front. Immunol.* **11**, 896 (2020).
30. Corradi, D., Callegari, S., Maestri, R., Benussi, S. & Alfieri, O. Structural remodeling in atrial fibrillation. *Nat. Clin. Pract. Cardiovasc. Med.* **5**, 782–796 (2008).
31. Ishii, Y. et al. Detection of fibrotic remodeling of epicardial adipose tissue in patients with atrial fibrillation: imaging approach based on histological observation. *Heart Rhythm O2* **2**, 311–323 (2021).
32. van den Berg, N. W. E. et al. Epicardial and endothelial cell activation concurs with extracellular matrix remodeling in atrial fibrillation. *Clin. Transl. Med.* **11**, e558 (2021).
33. Haemers, P. et al. Atrial fibrillation is associated with the fibrotic remodelling of adipose tissue in the subepicardium of human and sheep atria. *Eur. Heart J.* **38**, 53–61 (2017).
34. Zhou, B. & Tian, R. Mitochondrial dysfunction in pathophysiology of heart failure. *J. Clin. Invest.* **128**, 3716–3726 (2018).
35. Grant, R. W. & Dixit, V. D. Adipose tissue as an immunological organ. *Obesity* **23**, 512–518 (2015).
36. Cyganek, L. et al. Deep phenotyping of human induced pluripotent stem cell-derived atrial and ventricular cardiomyocytes. *JCI Insight* **3**, e99941 (2018).
37. Sobie, E. A., Song, L. S. & Lederer, W. J. Restitution of Ca^{2+} release and vulnerability to arrhythmias. *J. Cardiovasc. Electrophysiol.* **17**, S64–S70 (2006).
38. Kim, J. A., Chelu, M. G. & Li, N. Genetics of atrial fibrillation. *Curr. Opin. Cardiol.* **36**, 281–287 (2021).
39. Tzialla, C. et al. *SCN2A* and arrhythmia: a potential correlation? A case report and literature review. *Eur. J. Med. Genet.* **65**, 104639 (2022).
40. Heras-Bautista, C. O. et al. Cardiomyocytes facing fibrotic conditions re-express extracellular matrix transcripts. *Acta Biomater.* **89**, 180–192 (2019).

41. Zeemering, S. et al. Atrial fibrillation in the presence and absence of heart failure enhances expression of genes involved in cardiomyocyte structure, conduction properties, fibrosis, inflammation, and endothelial dysfunction. *Heart Rhythm* **19**, 2115–2124 (2022).
42. Huang, J. et al. Plasma level of interferon-γ predicts the prognosis in patients with new-onset atrial fibrillation. *Heart Lung Circ.* **29**, e168–e176 (2020).
43. Ashour, D. et al. An interferon gamma response signature links myocardial aging and immunosenescence. *Cardiovasc. Res.* **119**, 2458–2468 (2023).
44. Iacobellis, G. Epicardial adipose tissue in contemporary cardiology. *Nat. Rev. Cardiol.* **19**, 593–606 (2022).
45. Lenz, M., Arts, I. C. W., Peeters, R. L. M., de Kok, T. M. & Ertaylan, G. Adipose tissue in health and disease through the lens of its building blocks. *Sci. Rep.* **10**, 10433 (2020).
46. Ryan, G. E., Harris, J. E., Richmond, J. M. & Resident Memory, T. Cells in autoimmune skin diseases. *Front. Immunol.* **12**, 652191 (2021).
47. Chang, M. H. et al. Arthritis flares mediated by tissue-resident memory T cells in the joint. *Cell Rep.* **37**, 109902 (2021).
48. Lazzerini, P. E., Abbate, A., Boutjdir, M. & Capecchi, P. L. Fir(e)ing the rhythm: inflammatory cytokines and cardiac arrhythmias. *JACC Basic Transl. Sci.* **8**, 728–750 (2023).
49. Wang, F., Wei, Q. & Wu, X. Cardiac arrhythmias associated with immune checkpoint inhibitors: a comprehensive disproportionality analysis of the FDA adverse event reporting system. *Front. Pharmacol.* **13**, 986357 (2022).
50. Fung, H. Y., Teryek, M., Lemenze, A. D. & Bergsbaken, T. CD103 fate mapping reveals that intestinal $CD103^-$ tissue-resident memory T cells are the primary responders to secondary infection. *Sci. Immunol.* **7**, eabl9925 (2022).
51. Weisberg, S. P. et al. Tissue-resident memory T cells mediate immune homeostasis in the human pancreas through the PD-1/PD-L1 pathway. *Cell Rep.* **29**, 3916–3932 (2019).
52. Jaiswal, A. et al. An activation to memory differentiation trajectory of tumor-infiltrating lymphocytes informs metastatic melanoma outcomes. *Cancer Cell* **40**, 524–544 (2022).
53. Mami-Chouaib, F. et al. Resident memory T cells, critical components in tumor immunology. *J. Immunother. Cancer* **6**, 87 (2018).
54. Sasson, S. C. et al. Interferon-gamma–producing $CD8^+$ tissue resident memory T cells are a targetable hallmark of immune checkpoint inhibitor–colitis. *Gastroenterology* **161**, 1229–1244 (2021).
55. Joseph, L. et al. Incidence of cancer treatment induced arrhythmia associated with immune checkpoint inhibitors. *J. Atr. Fibrillation* **13**, 2461 (2021).
56. Liu, L. et al. PD-1/PD-L1 expression on CD^{4+} T cells and myeloid DCs correlates with the immune pathogenesis of atrial fibrillation. *J. Cell. Mol. Med.* **19**, 1223–1233 (2015).
57. Venteclef, N. et al. Human epicardial adipose tissue induces fibrosis of the atrial myocardium through the secretion of adipo-fibrokines. *Eur. Heart J.* **36**, 795–805 (2015).
58. Ernault, A. C. et al. Secretome of atrial epicardial adipose tissue facilitates reentrant arrhythmias by myocardial remodeling. *Heart Rhythm* **19**, 1461–1470 (2022).
59. Bénézech, C. et al. Inflammation-induced formation of fat-associated lymphoid clusters. *Nat. Immunol.* **16**, 819–828 (2015).
60. Zhang, X. Z. et al. T lymphocyte characteristics and immune repertoires in the epicardial adipose tissue of heart failure patients. *Front. Immunol.* **14**, 1126997 (2023).
61. Santema, B. T. et al. Pathophysiological pathways in patients with heart failure and atrial fibrillation. *Cardiovasc. Res.* **118**, 2478–2487 (2021).
62. Yao, Y., Yang, M., Liu, D. & Zhao, Q. Immune remodeling and atrial fibrillation. *Front. Physiol.* **13**, 927221 (2022).
63. Mitrokhin, V. et al. L-type Ca^{2+} channels' involvement in IFN-γ-induced signaling in rat ventricular cardiomyocytes. *J. Physiol. Biochem.* **75**, 109–115 (2019).
64. Dusi, V., Ghidoni, A., Ravera, A., De Ferrari, G. M. & Calvillo, L. Chemokines and heart disease: a network connecting cardiovascular biology to immune and autonomic nervous systems. *Mediators Inflamm.* **2016**, 5902947 (2016).
65. Hearnden, R., Sandhar, B., Vyas, V. & Longhi, M. P. Isolation of stromal vascular fraction cell suspensions from mouse and human adipose tissues for downstream applications. *STAR Protoc.* **2**, 100422 (2021).
66. Peacock, T., Heather, J. M., Ronel, T. & Chain, B. Decombinator V4: an improved AIRR compliant-software package for T-cell receptor sequence annotation? *Bioinformatics* **37**, 876–878 (2021).
67. Longhi, P. & Vyas, V. Bulk TCR-seq from paired EAT, atrial appendage and blood samples. *Zenodo* https://doi.org/10.5281/zenodo.13318819 (2024).

Acknowledgements

We are indebted to all the individuals who kindly agreed to participate in this study. We thank all members of the Barts Heart Centre, the Barts Bioresource staff, S. Petersen and M. Burton who assisted with participant consent and access to medical records. This work was supported by Barts Charity MGU0413 (V.V. and M.P.L.); Abbott (V.V. and M.C.F.); Medical Research Council MR/T008059/1 (V.V.); British Heart Foundation FS/19/62/34901 (B.B.); British Heart Foundation FS/13/49/30421 (M.P.L. and H.B.) and PG/16/79/32419 (E.G.W.); the NIHR Barts Biomedical Research Centre (M.C.F.); British Heart Foundation FS/4yPhD/F/22/34174B (J.M.K.); British Heart Foundation Accelerator Award AA/18/5/34222 (F.M.-B. and for purchasing of the CytoFLEX flow cytometer); and the Rosetrees Trust and the UCLH Biomedical Research Centre (B.C.).

Author contributions

M.P.L. conceived the study. V.V. and M.P.L. designed experiments. V.V., H.B., E.G.W. and B.S. collected processed tissue samples. V.V. performed and analyzed experiments. J.M.K. performed co-culture experiments. S.F. and F.M.-B. provided support for tissue imaging. E.S., J.W., A.J. and A.T. helped with iPSC-CM culture, characterization and electrophysiology studies. M.E. and N.M. supported deconvolution analysis. H.L.N. and N.F. performed RNA sequencing analysis. G.N., S.B. and B.C. performed bulk TCR sequencing analysis. M.P.L. wrote the paper.

Competing interests

The authors declare no competing interests.

Additional information

Extended data is available for this paper at https://doi.org/10.1038/s44161-024-00532-x.

Supplementary information The online version contains supplementary material available at https://doi.org/10.1038/s44161-024-00532-x.

Correspondence and requests for materials should be addressed to M. Paula Longhi.

Peer review information *Nature Cardiovascular Research* thanks Stephane Hatem, Klaus Ley, Na Li and the other, anonymous, reviewer(s) for their contribution to the peer review of this work.

Reprints and permissions information is available at www.nature.com/reprints.

Publisher's note Springer Nature remains neutral with regard to jurisdictional claims in published maps and institutional affiliations.

Open Access This article is licensed under a Creative Commons Attribution 4.0 International License, which permits use, sharing, adaptation, distribution and reproduction in any medium or format, as long as you give appropriate credit to the original author(s) and the source, provide a link to the Creative Commons licence, and indicate if changes were made. The images or other third party material in this article are included in the article's Creative Commons licence, unless indicated otherwise in a credit line to the material. If material is not included in the article's Creative Commons licence and your intended use is not permitted by statutory regulation or exceeds the permitted use, you will need to obtain permission directly from the copyright holder. To view a copy of this licence, visit http://creativecommons.org/licenses/by/4.0/.

© The Author(s) 2024

https://doi.org/10.1038/s44161-024-00532-x

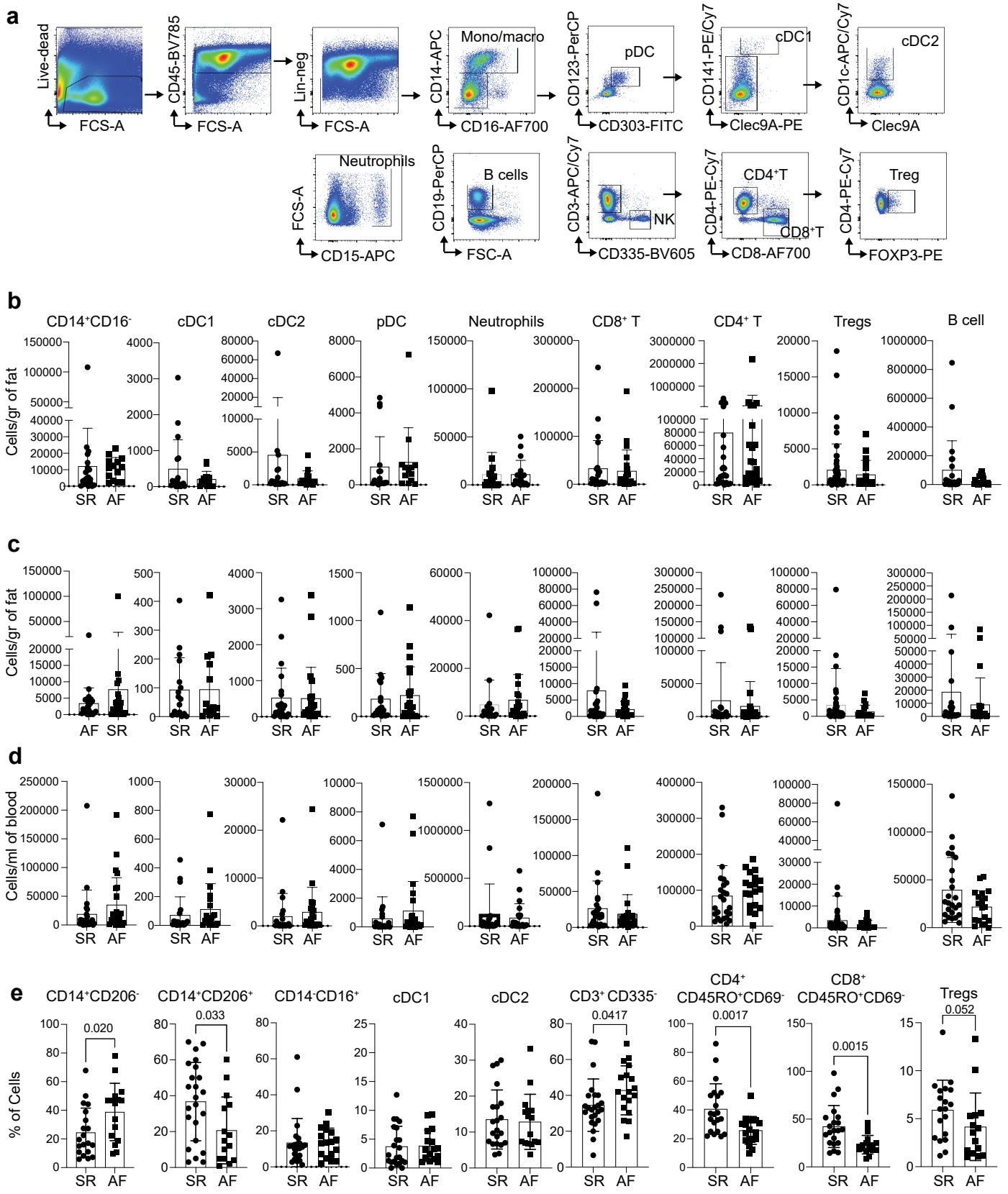

Extended Data Fig. 1 | Immune profiling of EAT. a. Gating strategy for the identification of lymphoid and myeloid cells in tissue. **b-d**. Absolute number of immune cells in patients with AF and on SR across EAT (**b**), SAT (**c**) and blood (**d**). **e**. Percentages of myeloid and lymphoid cells in the EAT. Statistical significance was determined by the unpaired two-tailed Mann-Whitney test, and data are represented as Mean ± SD. **b-e**. Data shows individual patients (n=26 SN and 18 AF biological replicates).

https://doi.org/10.1038/s44161-024-00532-x

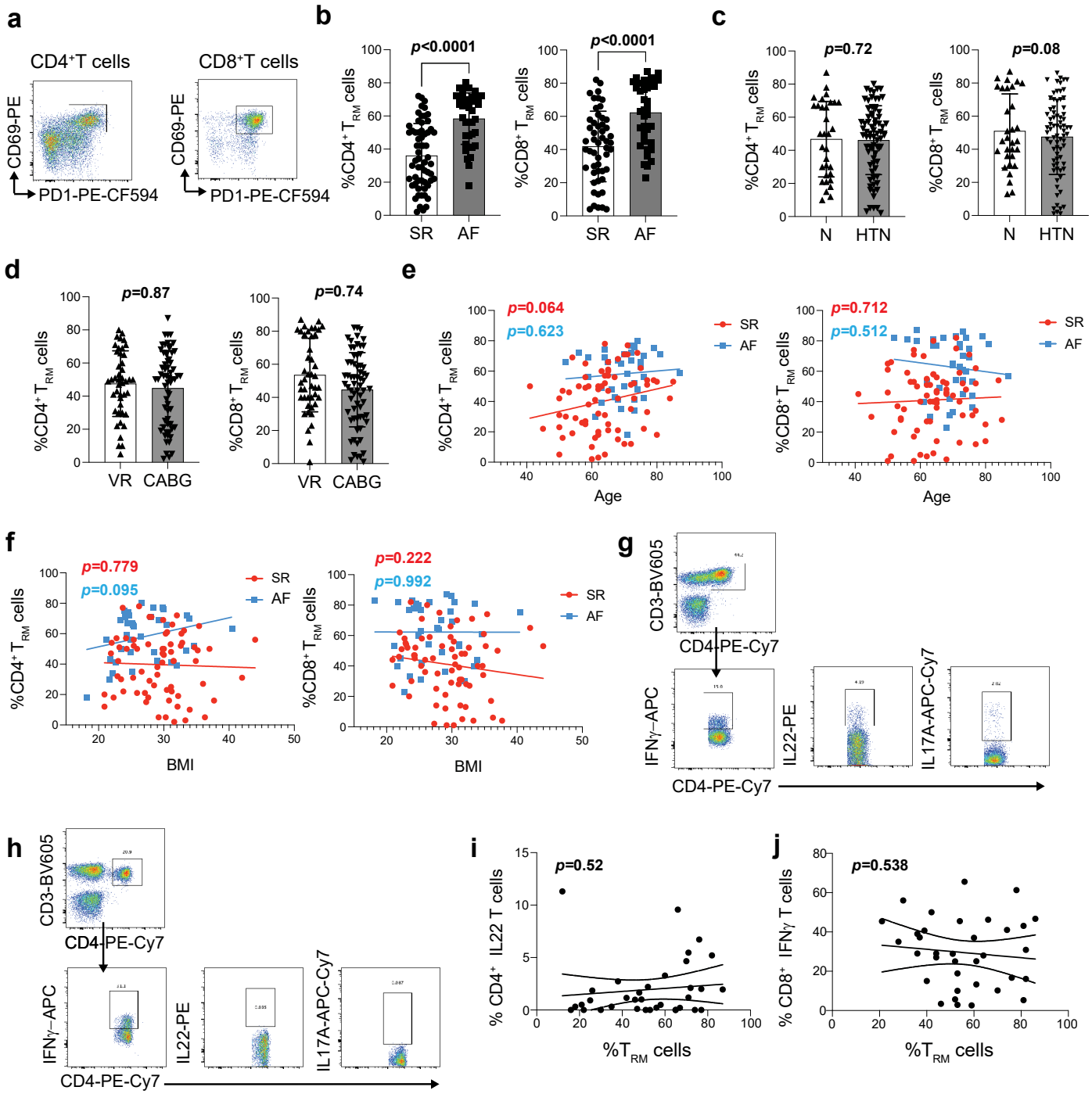

Extended Data Fig. 2. | Frequency of T_{RM} cells in AF. a. Gating strategy for the identification of T_{RM} cells. Immune cells were gated on live $CD3^+CD4^+$ or $CD8^+$ T cells as shown in Extended Data Fig. 1a. **b.** Frequency of $CD4^+$ and $CD8^+$ T_{RM} cells in unmatched patients with AF compared to SR controls. Patients with post-operative AF were excluded. **c.** Frequency of $CD4^+$ and $CD8^+$ T_{RM} cells in normotensive (N) compared to hypertensive (HTN) patients. **d.** Frequency of $CD4^+$ and $CD8^+$ T_{RM} cells between patients undergoing VR or CABG surgery. **b-d.** Significance was obtained using two-tailed Mann-Whitney test. Data is represented as Mean ± SD **e-f.** Correlation analysis of $CD4^+$ and $CD8^+$ T_{RM} cells with age (**d**) and BMI (**e**) by lineal regression and two-tailed p-value analysis. **g-h.** Gating strategy for the identification of cytokine production by $CD4^+$ (**f**) or $CD8^+$ (**g**) T cells T_{RM} cells. **i.** Correlation analysis of IL22 production with the frequency of $CD4^+$ T_{RM} cells measured by lineal regression and two-tailed p-value analysis. **j.** Correlation analysis of IFNγ production with the frequency of $CD8^+$ T_{RM} cells measured by lineal regression and two-tailed p-value analysis. **b-i.** Data shows individual patients (n=122).

https://doi.org/10.1038/s44161-024-00532-x

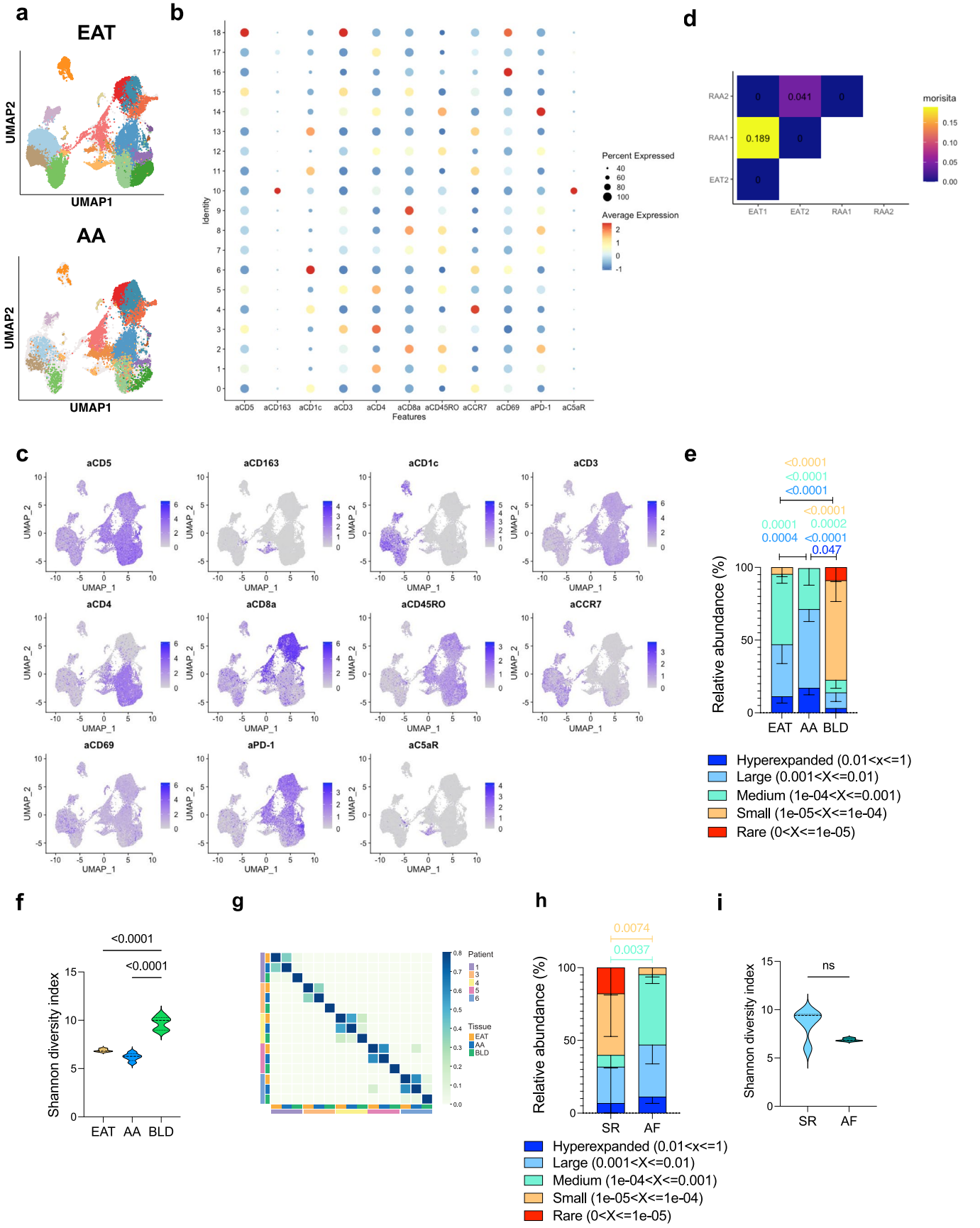

Extended Data Fig. 3 | See next page for caption.

https://doi.org/10.1038/s44161-024-00532-x

Extended Data Fig. 3 | Distinct protein profile across immune cells in EAT and AA. a. UMAP plots of EAT and AA samples identifying similar 19 cell clusters. **b**. Bubbleplotshowing surface expression of antibody-derived tag protein expression value for selective markers. **c**. UMAP plot representation of antibody-derived tag protein expression value for selective markers for the identification of memory T cells, B and myeloid cells. Colour bar key represents average expression levels. Expression values are normalized for quantitative comparison within each dataset. **d**. TCR clonal overlap detected by the Morisita index. **e**. Bar graph indicates the relative abundance of TCRβ clonotypes in paired tissues EAT, AA and Blood (BLD). The relative abundance of TCRβ clonotypes. **f**. TCRβ diversity between paired tissues. Statistical significance was evaluated with 2-way Anova followed Benjamini-Hochberg-correction. **g**. Heatmap illustrating the compositional TCRβ similarity between paired samples assessed using the Morisita-Horn index. Colour bar key represents the Morisita index. **h**. Bar graph indicates the relative abundance of TCRβ clonotypes between patients with AF and on SR. Data are presented as mean values ± SD. **e**-**h**. Statistical significance was evaluated using 2-way ANOVA with Sidak's multiple comparisons test. **i**. TCRβ diversity between AF and SR patients. Statistical significance was evaluated using the two-tailed Mann-Whitney *U* test for nonparametric data and represented as mean± SD. **e**-**i**. Data are from 5 biological replicates.

https://doi.org/10.1038/s44161-024-00532-x

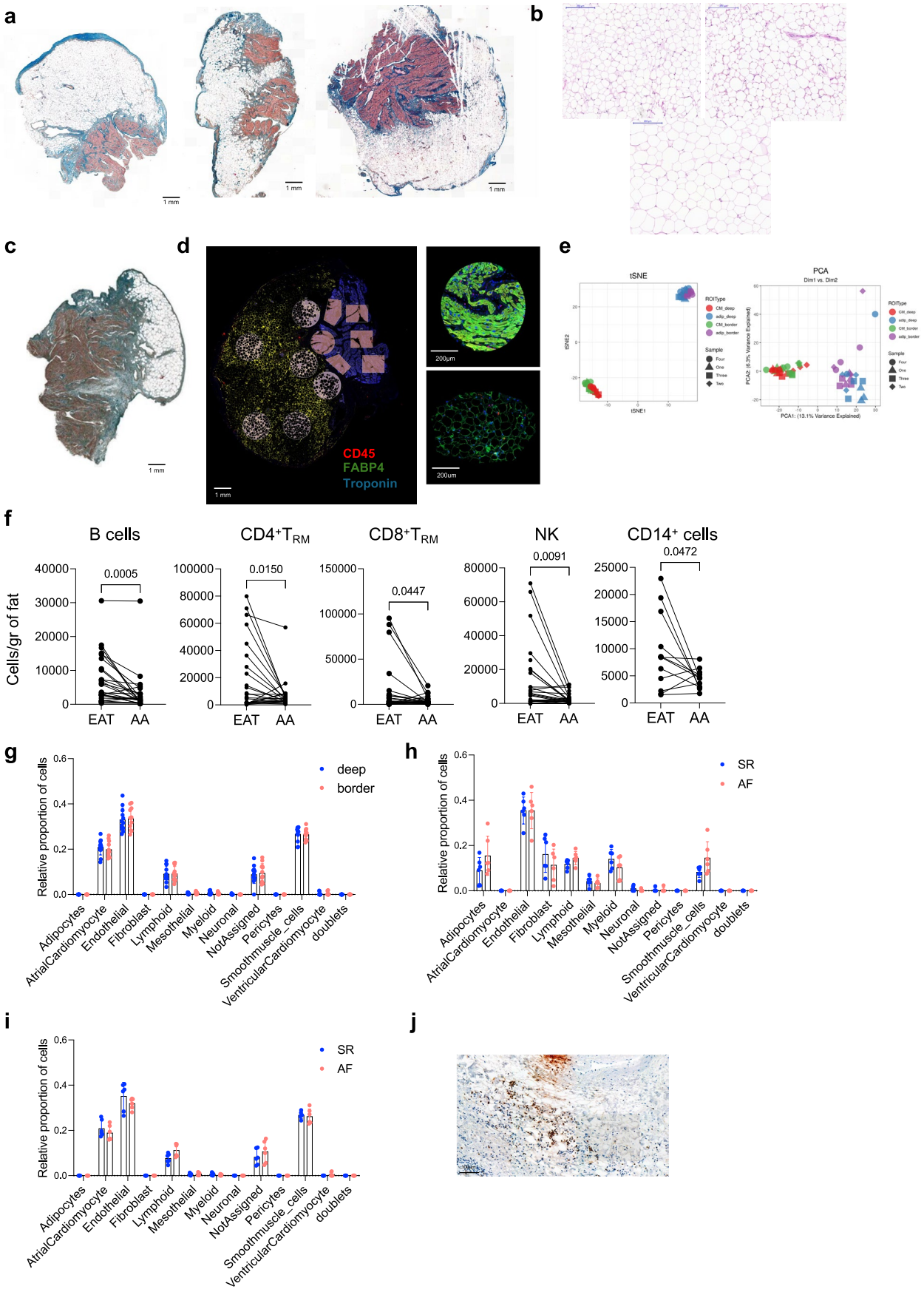

Extended Data Fig. 4 | See next page for caption.

https://doi.org/10.1038/s44161-024-00532-x

Extended Data Fig. 4 | Spatial transcriptomics. a. Representative Masson's Trichrome stains on tissue atrial specimens from 3 patients. **b**. Representative H&E stains on EAT specimens from 3 patients. **c**. Representative Masson's Trichrome stain on tissue specimen at 2.0x magnification with the blue colour depicting the collagen deposition in the EAT/RAA interface and red-brown the atrial tissue from 3 patients. **d**. Representative immunofluorescent staining used for the identification of regions of interest (ROI) for spatial transcriptomic analysis. Cardiomyocytes were identified by troponin staining (blue), adipocytes by FABP4 expression (green) and immune cells by CD45 (red). **e**. Dimensionality reduction plots demonstrating sample clustering by type of tissue. **f**. Absolute number of immune cells in paired EAT and AA tissue samples. Statistical significance was determined by paired two-tailed T test, and data are represented as mean± SD (n=18 biological replicates). **g**. Bar graph comparing the proportion of cell types over total populations between the AA borderzone and deep in the tissue. **h**-**i**. Bar graph comparing the proportion of cell types over total populations between the EAT (**h**) or AA (**i**) borderzoneand deep in the tissue between patients with AF and on SR. **g**-**h**. Statistical significance was evaluated by two-way ANOVA with Sidak's multiple comparison test. Bars represent mean±SD. **g**-**i**. Assays were performed in 3 biological replicates in technical triplicates. **j**. Representative immunohistochemistry staining of CCL5.

https://doi.org/10.1038/s44161-024-00532-x

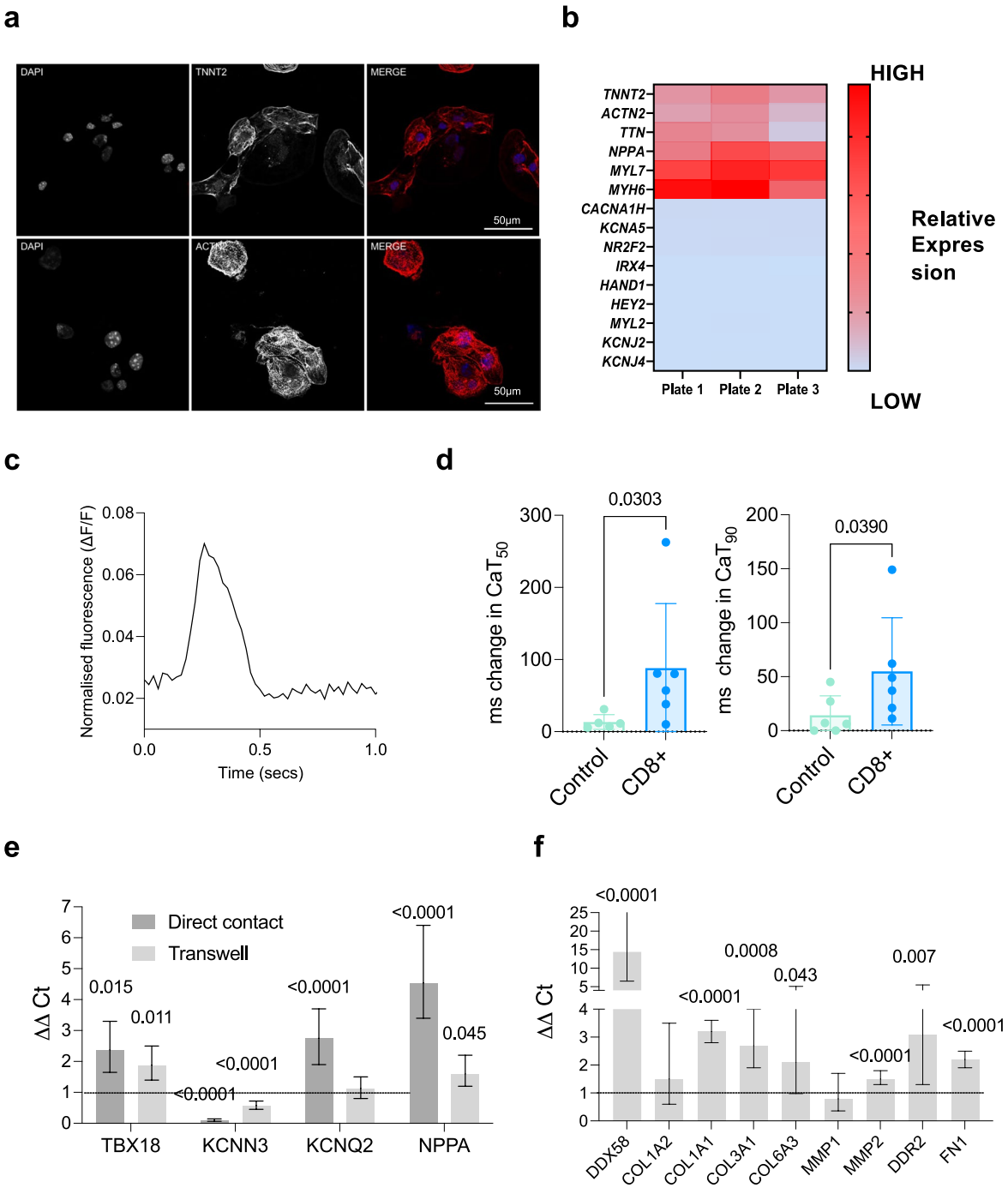

Extended Data Fig. 5 | Characterisation of iPSC-derived atrial cardiomyocytes. a. Representative immunofluorescence images depicting DAPI (nuclear stain), troponin (TNNT2) and smooth muscle actinin (ACTN2), and the merged images (DAPI) in blue, TNNT2 and ACTN2 in red). Scale bar 50 μM (3 independent experiments). **b.** Heat map demonstrating the relative expression of key atrial cardiomyocyte genes in independently differentiated cardiomyocyte plates (n=3). **c.** Atrial cardiomyocyte action potential waveform recorded using the voltage-sensitive dye, di-4-ANEPPS. **d.** Bar graphs demonstrating percentage change in CaT_{50} and CaT_{90} in $CD8^+$ T cells compared to untreated cells. Biological replicates n=6. Statistical significance was assessed using two-tailed t-test for parametric data, represented as mean and SD **e.** iPSC-cardiomyocytes were cultured directly with T_{RM} cells or in the presence of a 0.4 μM transwell were analysed by RT-PCR. Relative expression levels of selective genes in iPSC-cardiomyocytes (n = 6 biological replicates in triplicates) were analysed by RT-PCR. **f.** As in **e**, but bars represent expression of IFNγ–treated iPSC-cardiac fibroblast compared to untreated cells from three independently experiments (n = 9). **f-e.** Bars represent the mean ratio and upper and lower limits. Statistical significance was determined using unpaired two-tailed *t*-test.

nature portfolio

Corresponding author(s): Paula Longhi

Last updated by author(s): 14/05/2024

Reporting Summary

Nature Portfolio wishes to improve the reproducibility of the work that we publish. This form provides structure for consistency and transparency in reporting. For further information on Nature Portfolio policies, see our Editorial Policies and the Editorial Policy Checklist.

Statistics

For all statistical analyses, confirm that the following items are present in the figure legend, table legend, main text, or Methods section.

n/a	Confirmed	
☐	☒	The exact sample size (*n*) for each experimental group/condition, given as a discrete number and unit of measurement
☐	☒	A statement on whether measurements were taken from distinct samples or whether the same sample was measured repeatedly
☐	☒	The statistical test(s) used AND whether they are one- or two-sided *Only common tests should be described solely by name; describe more complex techniques in the Methods section.*
☐	☒	A description of all covariates tested
☐	☒	A description of any assumptions or corrections, such as tests of normality and adjustment for multiple comparisons
☐	☒	A full description of the statistical parameters including central tendency (e.g. means) or other basic estimates (e.g. regression coefficient) AND variation (e.g. standard deviation) or associated estimates of uncertainty (e.g. confidence intervals)
☒	☐	For null hypothesis testing, the test statistic (e.g. *F*, *t*, *r*) with confidence intervals, effect sizes, degrees of freedom and *P* value noted *Give P values as exact values whenever suitable.*
☒	☐	For Bayesian analysis, information on the choice of priors and Markov chain Monte Carlo settings
☒	☐	For hierarchical and complex designs, identification of the appropriate level for tests and full reporting of outcomes
☒	☐	Estimates of effect sizes (e.g. Cohen's *d*, Pearson's *r*), indicating how they were calculated

Our web collection on statistics for biologists contains articles on many of the points above.

Software and code

Policy information about availability of computer code

Data collection

Chromium Single Cell 5' v2 sequencing was processed using the Cell Ranger (version 6.0.1). FASTQ files were generated using cellranger mkfastq (v.6.01) and gene expression reads were aligned to the human reference genome GRCh38 and counted using cellranger count (v.6.01.) VDJ reads were aligned to the GRCh38 VDJ reference dataset using cellranger vdj (v.6.01).
For RNAseq analysis, Raw FASTQ files were first trimmed using trim-galore (version 0.6.7) and inspected for quality control using fastqc (version 0.11.9) and multiqc (version 1.12). Transcript and genome files were downloaded from GENCODE, release 43 (GRCh38.p13) to generate a decoy index files with Salmon (version 1.10.1). Salmon transcript quantifications were imported into R (version 4.1.0) to aggregate transcripts to genes using the package tximport (version 1.22.0)
For Bulk TCR-seq analysis, TCR identification, error correction and CDR3 extraction was performed following a suite of tools available at github.com/innate2adaptive/Decombinator .

Data analysis	Expression matrices were analysed using the Seurat package257 (v4.0.03). DoubletFinder258 (v2.0.3) was employed for multiplet filtering. SCTransform259 (v0.3.2) was used for normalization and Seurat (v4.0.3) integration to remove batch effects. Analysis was performed using scRepertoire261 (v1.3.5) and STARTRAC262 (v0.1.0). Differential gene analysis was performed using DESeq2 (version 1.34.0). GSEA (version 4.3.2) was performed using normalized gene counts generated by DESeq2. Spatial transcriptomic data was analyzed using GeoMx® DSP Software v2.0. For spatial deconvolution, the_SpatialDecon_plugin.R (v1.2 Nanostring) was employed. TCR frequency and similarity was analysed using the Immunarch package in R (v1.0.0). Graphs were generated and analysed with GraphPad Prism version 8. Flow cytometry data was analysed with FlowJo version 10.

For manuscripts utilizing custom algorithms or software that are central to the research but not yet described in published literature, software must be made available to editors and reviewers. We strongly encourage code deposition in a community repository (e.g. GitHub). See the Nature Portfolio guidelines for submitting code & software for further information.

Data

Policy information about availability of data

All manuscripts must include a data availability statement. This statement should provide the following information, where applicable:

- Accession codes, unique identifiers, or web links for publicly available datasets
- A description of any restrictions on data availability
- For clinical datasets or third party data, please ensure that the statement adheres to our policy

CITE-seq RNA sequencing raw and processed data are deposited in the Gene Expression Omnibus (GEO) under the accession number GSE263154. CellRanger v.6.0.1 was used with default parameters to map all the data from the samples to the human reference genome (GRCh38- https://www.ncbi.nlm.nih.gov/datasets/genome/GCF_000001405.26/). Bulk TCR-sequencing data are available at Zenodo https://doi.org/10.21203/rs.3.rs-3366081/v1. Suite of tools for TCR sequencing analysis can be access at github.com/innate2adaptive/Decombinator. Spatial Transcriptomic raw sequencing data have been deposited in GEO with the accession number GSE261363. Spatial profiling was carried out using the NanoString Technologies GeoMx® Digital Spatial Profiler. iPSC-cardiomyocytes RNA-seq datasets been submitted to GEO with the accession number GSE256520. Additional data generated in this study are provided in the Supplementary Information and Source Data sections.

Research involving human participants, their data, or biological material

Policy information about studies with human participants or human data. See also policy information about sex, gender (identity/presentation), and sexual orientation and race, ethnicity and racism.

Reporting on sex and gender	Information on sex has been collected and reported in the manuscript (clinical characteristics). Diabetes, hypertension, obesity, sleep-related breathing disorders, heart failure and ischaemic heart disease increase the risk of AF development/ persistence with many of these risk factors being more prevalent in male, thus the higher proportion of males in our clinical cohort. For this reason, sex-based analysis was not possible due to low power. Informed consent was obtained for all patients.
Reporting on race, ethnicity, or other socially relevant groupings	Although ethnicity information was obtained for most our patients, this was not reported in the study. Atrial Fibrillation (AF) is more prevalence among Caucasians compared with Blacks, and Asians and, therefore, 82% of our patients were white.
Population characteristics	all the covariant-relevant characteristics are indicated in the clinical characteristics (Supplementary Table 1) and were taking into consideration during propensity matching. APatients were matched for age, gender, BMI, diabetes, hypertension and procedure type (CABG/VR). Atrial fibrillation risk increases with age and metabolic syndrome (obesity, diabetes and metabolic syndrome). AF is common in participants with valvulopaties and affects more male than females.
Recruitment	Participants were selected based on inclusion and exclusion criteria. Inclusion criteria: Adult Adult (≥18 years) patients, undergoing on-pump open chest coronary artery bypass grafting (CABG) surgery, valve surgery or combined CABG/valve surgery were consented prior heart surgery at Barts Heart Centre, St Bartholomew's Hospital (London, UK) . Exclusion criteria included: congenital heart disease, underlying cardiomyopathies or ion channelopathies, primarily undergoing other cardiac surgical procedures (e.g. aortic surgery), off-pump CABG surgery, patients with active endocarditis, myocarditis or pericarditis, those with pre-existing inflammatory diseases (e.g. rheumatoid arthritis), active malignancy, patients on immunomodulatory or biologic drugs (e.g. tacrolimus, anti-TNF-α agents), peri-operative rhythm control therapies e.g. use of amiodarone, post-operative haemodynamic shock, uncorrected potassium derangement (K<3.3 or K>5.8) or uncorrected magnesium derangement (Mg<0.5 or Mg>1.5) detected on laboratory blood sample analysis. No other selection criteria were employed . Participants were consented prior surgery. The Barts Heat Centre is one of the largest cardiac unit in Europe serving an ethnically diverse community and therefore not all of them speak and/or read English. Experienced translators and English speaking family members were present at the time of consent to limit sampling biases. However, despite the diverse population, this is a single-centre study which could bias towards a population with specific clinical characteristics.
Ethics oversight	East of England - Cambridge Central Research Ethics Committee (REC). Participants were screened and gave informed written consent for study participation as per local research procedures and Good Clinical Practice guidance through the Barts BioResource (Research Ethics Committee reference: 14/EE/0007).

Note that full information on the approval of the study protocol must also be provided in the manuscript.

Field-specific reporting

Please select the one below that is the best fit for your research. If you are not sure, read the appropriate sections before making your selection.

☒ Life sciences ☐ Behavioural & social sciences ☐ Ecological, evolutionary & environmental sciences

For a reference copy of the document with all sections, see nature.com/documents/nr-reporting-summary-flat.pdf

Life sciences study design

All studies must disclose on these points even when the disclosure is negative.

Sample size	Power calculations were based on the percentage of Trm cells, with CD4+TRM cells giving the higher effector size. Power calculations were calculated using T-test, with a mean of 37.8 and 56.5 and SD of 20.3, and to achieve a power of 0.8 with a significant level of 0.05. For in vitro Trm cultures, power calculations were based in published data in Bourdely P et al. doi: 10.1016/j.immuni.2020.06.002, requiring n=5 donors/ condition (Effect size 2.96, alpha error 0.05 and 95% power)
Data exclusions	Participant on sinus rhythm (SR) prior surgery were monitored during hospital stay for the development of Post-operative AF (POAF), defined as an ECG of >30seconds of AF during the 7-day post-operative period. Those that developed POAF were excluded post data acquisition from the study as they could not be classified as SR any longer.
Replication	As this is a clinical observational study, with limited human sample collection, reproducibility of our findings were based on the use of different technical approaches to confirm the initial findings obtained with flow cytometry. Data are based on biological replicates with flow cytometry performed on 153 participants (72 after propensity matching). In vitro co-cultured assays were performed with 5 biological replicates in three experimental repeats. Bulk TCR-seq and RAN-sea analysis were performed in 5 biological repeats.
Randomization	No randomization was applied as was not applicable to the study. Covariants were controlled with propensity matching.
Blinding	Patients samples were labeled with nonidentifying numbers and sample analysis was performed blindly by two investigators.

Reporting for specific materials, systems and methods

We require information from authors about some types of materials, experimental systems and methods used in many studies. Here, indicate whether each material, system or method listed is relevant to your study. If you are not sure if a list item applies to your research, read the appropriate section before selecting a response.

Materials & experimental systems

n/a	Involved in the study
☐	☒ Antibodies
☐	☒ Eukaryotic cell lines
☒	☐ Palaeontology and archaeology
☒	☐ Animals and other organisms
☒	☐ Clinical data
☒	☐ Dual use research of concern
☒	☐ Plants

Methods

n/a	Involved in the study
☒	☐ ChIP-seq
☐	☒ Flow cytometry
☒	☐ MRI-based neuroimaging

Antibodies

Antibodies used

TotalSeq antibodies were purchased from Biolegend.
TotalSeq™-C0138 anti-human CD5 (1:200); clone: UCHT2; CAT: 300637; Lot: B309305
TotalSeq™-C0358 anti-human CD163 (1:200); clone: GHI/61; Cat: 333637; Lot: B322549
TotalSeq™-C0160 anti-human CD1c (1:200); Clone: L161; Cat: 331547; Lot: B306006
TotalSeq™-C0049 anti-human CD3 (1:200); Clone: SK7; Cat: 344849; Lot: B306005
TotalSeq™-C0072 anti-human CD4 (1:200); Clone: RPA-T4; Cat: 300567; Lot: B310155
TotalSeq™-C0080 anti-human CD8a (1:200); Clone: RPA-T8: Cat: 301071; Lot: B315106
TotalSeq™-C0087 anti-human CD45RO (1:100); Clone: UCHL1; Cat: 304259; Lot: B335899
TotalSeq™-C0148 anti-human CD197 (1:100),Clone: G043H7; Cat: 353251; Lot: B330975
TotalSeq™-C0146 anti-human CD69 (1:100); Clone: FN50; Cat: 310951; Lot: B337757
TotalSeq™-C0088 anti-human CD279 (1:100); Clone: EH12.2H7; Cat: 329963; Lot: B313421
TotalSeq™-C1046 anti-human CD88 (1:200); Clone: S5/1; Cat: 344319; Lot: B306415
Addition antibodies
CD197-FITC (Biolegend, Cat: 353216,1:200 dilution, clone 353216), CD19-PerCP-Cy5.5 (Biolegend, Cat 302228, Clone H1B19, 1:200 dilution), CD45RO-BV421 (Biolegend, Cat 304224,Clone UCHL1, 1:200 dilution), CD335-BV605 (Biolegend, Cat 331926, Clone 9E2, 1:200 dilution), CD45-BV785 (Biolegend, Cat 304048, Clone HI30, Lot B284678, 1:200 dilution), CD127-APC (Biolegend, Cat 351342, Clone A019D5, Lot B280742 1:200 dilution), CD8-AF700 (Biolegend, Cat 300920, CloneHIT8a, 1:500 dilution), CD3-APC/Cy7 (Biolegend, Cat 300318, Clone HIT3a, 1:200 dilution), CD69-PE (Biolegend, Cat 310906,Clone FN50, 1:200 dilution), CD4-PE/Cy7

(Biolegend, cat 357410, Clone A161A1, 1:200 dilution), PD1-PE-CF594 (Biolegend, cat 329940, Clone EH12.2H7, 1:200 dilution), KLRG1-SB702 (eBioscience, Cat 15824202, Clone 13F12F2 1:200 dilution), CD303-FITC (Biolegend, Cat 354208, Clone 201A, 1:200 dilution), CD123-PerCP/Cy5.5 (Biolegend, Cat 306016, Clone 6H6, 1:200 dilution), CD206-BV421 (Biolegend, Cat 321126, Clone 15-2 1:200 dilution), CD3-BV605 (Biolegend, Cat 317322, Clone OKT3, 1:200 dilution), CD19-BV605 (Biolegend, Cat 302244, Clone HIB19, 1:200 dilution), CD14-APC (Biolegend, Cat 325608, Clone HCD14, 1:200 dilution), CD16-AF700 (Biolegend, Cat 302026, Clone 3G8, 1:500 dilution), CD1c-APC/Cy7 (Biolegend, Cat 331520, Clone L1G1, 1:200 dilution), Clec9A-PE (Biolegend, Cat 353804, Clone 8F9, 1:200 dilution), CD1a-PE-CF594 (Biolegend, Cat 300132, Clone H149, 1:200 dilution), and CD141-PE/Cy7 (Biolegend, Cat 344110,Clone M80, 1:200 dilution), IFNg-APC (Biolegend, Cat 502511, Clone 4S.B3, 1:200 dilution), IL17-APC/Cy7 (Biolegend, Cat 512319, Clone BL168, 1:200 dilution), IL22-PE (Biolegend, Cat 366703, Clone 2G12A41, 1:200 dilution).

Validation

Antibodies were previously validated in Vyas et al. (PMID: 34283808). Total-seq antibodies were validated by flow cytometry using the same fluorescent-labeled antibody clones.

Eukaryotic cell lines

Policy information about cell lines and Sex and Gender in Research

Cell line source(s)	HipSci deposited by the Wellcome Trust Sanger institute into the Culture Collections archive (UK Health Security Agency, UK).
Authentication	Atrial phenotype upon differentiation was validated by gene expression profile and electrical changes.
Mycoplasma contamination	negative
Commonly misidentified lines (See ICLAC register)	No Misidentified Cell Lines were used in the study

Flow Cytometry

Plots

Confirm that:

☒ The axis labels state the marker and fluorochrome used (e.g. CD4-FITC).

☒ The axis scales are clearly visible. Include numbers along axes only for bottom left plot of group (a 'group' is an analysis of identical markers).

☒ All plots are contour plots with outliers or pseudocolor plots.

☒ A numerical value for number of cells or percentage (with statistics) is provided.

Methodology

Sample preparation	AA samples were enzymatically digested with 675U collagenase I (Sigma-Aldrich), 187.5U collagenase XI (Sigma-Aldrich) and 10U DNase (Sigma-Aldrich) in 1ml of Hanks' buffered salt solution at 37°C with 225rpm agitation for 45 mins. Adipose tissue samples were digested with Collagenase II and DNase at 37°C with 225rpm agitation for 30 mins. PBMCs were isolated using Ficoll-Paque PLUS (Cytiva) as per manufacturer's instructions. Single cell suspensions were obtained following centrifugation and red cell lysing prior to antibody staining
Instrument	Data was acquired on a Cytoflex (Beckman Coulter)
Software	FlowJo version 10 software.
Cell population abundance	TRM cells comprise a 40 to 80% of CD4+ or CD8+ T cell respectively and proximately a 20-30% of immune cells. Post-sort purity was assessed by sorted cell analysis by LSR Fortessa analyzer.
Gating strategy	Gating strategy is defined in the supplementary data.

☒ Tick this box to confirm that a figure exemplifying the gating strategy is provided in the Supplementary Information.